Coupling the fictitious domain and sharp interface methods for the simulation of convective mass transfer around reactive particles: Towards a reactive Sherwood number correlation for dilute systems

Mostafa Sulaiman, Abdelkader Hammouti, Anthony Wachs, Eric Climent

Coupling the fictitious domain and sharp interface methods for the simulation of convective mass transfer around reactive particles: towards a reactive Sherwood number correlation for dilute systems

Mostafa Sulaiman[a], Abdelkader Hammouti[a], Eric Climent[b], Anthony Wachs[c,d,*]

[a] *IFP Énergies Nouvelles, Fluid Mechanics Department, Rond-point de l'échangeur de Solaize, BP 3, 69360 Solaize, France*
[b] *Institut de Mécanique des Fluides de Toulouse (IMFT) Université de Toulouse,CNRS - Toulouse, France*
[c] *Department of Mathematics, University of British Columbia, 1984 Mathematics Road, Vancouver, BC V6T 1Z2, Canada*
[d] *Department of Chemical and Biological Engineering, University of British Columbia, 2360 East Mall, Vancouver, BC V6T 1Z3, Canada*

Abstract

We suggest a reactive Sherwood number model for convective mass transfer around reactive particles in a dilute regime. The model is constructed with a simple external-internal coupling and is validated with Particle-Resolved Simulation (PRS). The PRS of reactive particle-fluid systems requires numerical methods able to handle efficiently sharp gradients of concentration and potential discontinuities of gradient concentrations at the fluid-particle interface. To simulate mass transfer from reactive catalyst beads immersed in a fluid flow, we coupled the Sharp Interface Method (SIM) to a Distributed Lagrange Multiplier/Fictious Domain (DLM/FD) two-phase flow solver. The accuracy of the numerical method is evaluated by comparison to analytic solutions and to generic test cases fully resolved by boundary fitted simulations. A previous theoretical model that couples the internal diffusion-reaction problem with the external advection-diffusion mass transfer in the fluid phase is extended to the configuration of three aligned spherical particles representative of a dilute particle-laden flow. Predictions of surface concentration, mass transfer coefficient and chemical effectiveness factor of catalyst particles are validated by DLM-FD/SIM simulations. It is shown that

*Corresponding author
Email address: wachs@math.ubc.ca (Anthony Wachs)

the model captures properly the effect of an internal first order chemical reaction on the overall respective reactive Sherwood number of each sphere depending on their relative positions. The proposed correlation for the reactive Sherwood number is based on an existing non-reactive Sherwood number correlation. The model can be later used in Euler/Lagrange or Euler/Euler modelling of dilute reactive particle-laden flows.

Keywords: Sharp Interface Method, Catalyst particle, Mass transfer, Sherwood number, Chemical reaction, Thiele modulus.

Graphical Abstract

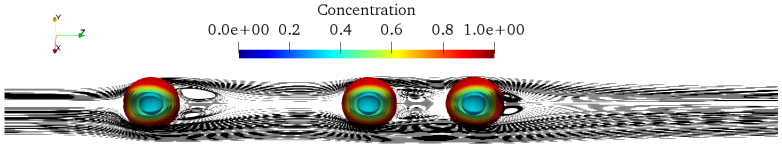

(a) $Re = 50, \gamma = 0.1, Sc = 1$ and $\phi^2 = 40$

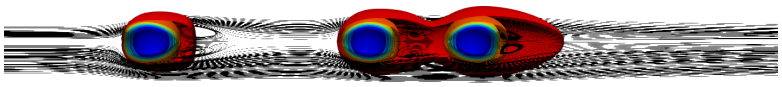

(b) $Re = 50, \gamma = 0.1, Sc = 1$ and $\phi^2 = 200$

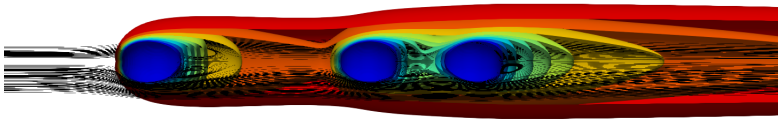

(c) $Re = 50, \gamma = 0.1, Sc = 1$ and $\phi^2 = \infty$

1. Introduction

Systems involving interactions of a dispersed solid phase with a continuous fluid phase through momentum, heat and mass transfer are ubiquitous in a wide range of industrial and energetic processes. A classical process in the chemical enginering industry is catalytic cracking in a reactor. If the dispersed solid phase, commonly referred to as particles, is fixed in the reactor, the system is known as a fixed bed and the flow is relevant of the flow through a porous medium represented by the network of randomly stacked catalytic particles (Furuta et al., 2006). If particles are mobile, the system is known as a fluidized bed (Gidaspow, 1994; Montero et al., 2018). In both reactors, the fluid enters the system with an imposed concentration of reactants and reactants are transferred from fluid phase bulk to catalytic particles bulk through diffusion, where chemical reactions take place in the form of heterogeneously catalyzed gas or liquid reaction. The modeling, operation, design and optimization of these systems necessitate an advanced comprehension of the coupling among the dominant transfer phenomena, namely momentum, heat, and mass transfer, that are usually associated to the presence of chemical reactions. For decades, operating experimental setups and deriving simplified analytical solutions were the two only ways to improve the comprehension of these systems. With the emergence of robust, accurate and computationally efficient numerical approaches/methods, we can complement and extend our comprehension with, e.g., reliable information about the micro-scale interactions in these systems that are not accessible through experiments or theory.

Over the past two decades, diverse Computational Fluid Dynamics (CFD) approaches/methods for the simulation of systems involving fluid/solid interactions have been developed. Combined to the increasing power of supercomputers that now enables one to perform Direct Numerical Simulations (DNS) at the scale of particles, CFD tools are now capable of supplying reliable and high quality detailed data in the flow. In this class of highly resolved CFD methods, Particle Resolved Simulation (PRS) has arisen as a mature method able to provide reliable local information about momentum, heat and mass transfer at the particle scale in particulate flows (Sun et al. (2016) among many others). PRS methods can be classified into two categories:

(i) The first category comprises body-fitted mesh methods. The advantage of this type of method relies on the ease to enforce boundary conditions at the particle surface, i.e., at the fluid/particle interface. This technique has been used to investigate transport properties in a bed made of multiple fixed particles by Romkes et al. (2003); Augier et al. (2010a) and convective heat/mass transfer over a single particle by Feng and Michaelides (2000). It has also been employed for moving particles by Hu et al. (2001) and moving boundaries by Duarte et al. (2004).

(i) The second category comprises fixed mesh methods. The challenge of this type of method is the difficulty in enforcing the correct boundary conditions at the particle surface while the main advantage is the use of a regular cartesian grid. The Immersed Boundary Method (IBM) uses Lagrangian markers at the particle surface to impose boundary conditions and introduces an additional forcing term (Uhlmann, 2005). Xia et al. (2014) applied IBM to study convective heat/mass transfer over a single particle. IBM was also used to evaluate the heat transfer Nusselt number in dense particulate flow systems by Deen et al. (2014) and Sun et al. (2015). Both studies compared their results to the pioneering experimental work of Gunn (1978) and proposed corrections of Gunn's correlation based on their data sets. Recently, IBM has been used by Lu et al. (2018) to examine mass transfer in particulate flows with surface reaction. The Lattice Boltzmann Method (LBM) is another computational method that uses a fixed mesh. LBM has also been applied to particulate flows with heat transfer by Khiabani et al. (2010) and Kruggel-Emden et al. (2016). Unlike conventional discretization schemes that solve the classical conservation equations, LBM solves convection-collision steps of probability density functions. Finally, the Distributed Lagrange Multiplier / Fictitious Domain Method (DLM/FD), firstly introduced by Glowinski et al. (2001), combines the particle and fluid equations of motion into a single, weak, and general equation of motion called combined momentum equation. The combined equations are derived through the combined velocity space incorporating the rigid body motion (no-slip) in the particle. The DLM/FD method has been extended to treat heat/mass transfer by Yu et al. (2006), Dan and Wachs

(2010) and Wachs (2011).

Apart from Yu et al. (2006) that considered diffusion inside particles, the common feature of the aforementioned fixed-mesh methods is that they solve the convection-diffusion equation by enforcing a uniform temperature (or concentration) in the whole solid particle volume. This type of method is inadequate for the treatment of systems where temperature/concentration gradients are prominent within the particle. In this case, the convection-diffusion (or convection-diffusion-reaction) equation must be solved in both domains, i.e., in the solid domain and in the fluid domain. Augier et al. (2010b) used a Volume of Fluid method (VOF) to study the efficiency of partially-wetted stacked catalyst particles. Catalyst efficiency was studied for different particles shapes as a function of Thiele modulus. Haroun et al. (2010) employed a VOF method to study interfacial-reactive mass transfer in two-phase flows. Although efficient, the VOF method necessitates a highly refined mesh at interfaces in order to accurately enforce the correct boundary conditions, which may render, for a fixed Cartesian mesh, the method computationally inefficient due to the huge computational cost. The main drawback of the VOF method is that it is not capturing discontinuities.

The Sharp Interface Method (SIM), also referred to as Ghost Fluid Method (GFM), is a fixed-mesh numerical method used to accurately capture boundary conditions with discontinuities along embedded interfaces (Shi et al., 2011). In the SIM, jump conditions are incorporated in the discretization of the differential operators on the Cartesian grid in the vicinity of the interface. SIM was firstly introduced by Fedkiw et al. (1999) and employed to impose boundary conditions at a contact discontinuity in the inviscid Euler equations. SIM was later extended to treat more general discontinuities by Liu et al. (2000). In their work, Liu et al. (2000) developed a version of SIM to address the problem of inhomogeneous Poisson equation in the presence of interfaces. The method is easy to implement in three dimensions and the matrix associated to the discrete Laplacian operator remains symmetric, allowing to use 'black box' scientific libraries to solve the corresponding linear system. Gibou et al. (2002) considered the Poisson equation with a non-uniform coefficient and Dirichlet boundary conditions on an irregular domain and showed that a second order accuracy can be obtained with a

simple discretization scheme that also preserves the matrix symmetry. Udaykumar and Mao (2002) and Gibou et al. (2003) employed the SIM to track the evolution of solidification fronts in the presence of heat and solute transport in the dendritic solidification of aqueous salt solutions. Kang et al. (2000) extended the SIM to treat multiphase incompressible flows including effects of viscosity, surface tension and gravity and applied the method to two-phase water-air mixtures. Marella et al. (2005) used a SIM to simulate immersed boundary problems while Liu et al. (2005) simulated droplet interactions with objects of different shapes using a SIM that accounts for surface tension and viscosity jumps. Kapahi et al. (2013) used a modified SIM to treat interfaces of embedded objects, with an application to shock-wave particulate flows. Finally, to end this non-exhaustive list of SIM-related works, Shao et al. (2012) combined the SIM with a Fictitious Domain method to simulate heat transfer in particulate flows with heat diffusion inside particles.

PRS is very powerful to supply high quality data inside the flow but is still limited to up to a few thousands, at best a few tens of thousands, of particles due to the large computing cost of these simulations. Finely resolved simulations as PRS can easily comprise hundreds of millions, and even a few billions, of grid cells, that represent highly challenging parallel computing problems, whether on multi-CPU or the emerging GPU/multi-GPU technology. Thereby, from a modelling viewpoint, there has been a sustained appeal to combine these particle-scale models to larger scale models, namely Euler/Lagrange at the so-called meso scale and Eulere/Euler at the so-called macro scale. The conceptual features of a fully integrated multi-scale modeling of particle-laden flows is comprehensively described by Deen et al. (2014). The vast majority of the multi-scale approaches suggested in the field of particle-laden flows assume a bottom-up strategy or phrased in a more emphatic way an upwards cascade of knowledge. In short, what is learnt through highly resolved simulations at the micro scale on small representative systems is meant to be transferred to higher scale models and to contribute to a deeper understanding of the particle-laden flow dynamics. Among the assorted ways to transfer knowledge, the most popular way has undoubtedly been over the last 15 years to enhance existing correlations for dimensionless numbers representative of momentum, heat or mass transfer. Among many others,

Deen et al. (2014) and Sun et al. (2015) suggested corrections to enhance the Nusselt number correlation suggested by Gunn (1978) 30 years earlier. Our objective in this paper follows the same line, i.e., to suggest a new correlation or to enhance an existing correlation derived from micro scale PRS that can be later used in meso scale Euler/Lagrange and macro scale Euler/Euler modelling.

In the present study, we combine a Fictitious Domain method and a first order Sharp Interface method to investigate mass transfer in particulate flows in the presence of a first order reaction inside particles. The 3D simulation results supplied by this computational Method in a flow configuration representative of dilute particle-laden flows are used to assess the validity of a reactive Sherwood number correlation that we already suggested for the case of a single sphere in an unbounded domain in Sulaiman et al. (2018) and that we revisit later in this work. We intend to show that a reactive Sherwood number correlation can be constructed based on simple external-internal coupling. The obtained model relies on any non-reactive Sherwood number correlation available in the literature and is deemed to perform well. The rest of the paper is organized as follows. We shortly summarized in *Section 2* the equations and the corresponding dimensionless numbers governing the problem. *Section 3* elaborates on the features of our numerical method that combines a DLM/FD method to compute the flow field and a SIM to compute the chemical species concentration field. Then, we present in *Section 4* a series of validation tests of growing complexity involving a single sphere. We start with diffusion, then move on with diffusion-reaction, convection-diffusion, and finally consider convection-diffusion-reaction. In the last case, and due to the lack of analytical solutions and previously established correlations to compare our numerical results to, we perform a comparison between SIM and a body-fitted method that fully resolves the interface to investigate the efficiency of our SIM method and determine its limits of validity in terms of range of dimensionless parameters considered and grid size, through a series of convergence tests. We also show, through comparison in a diffusion-reaction case, the advantage of SIM over VOF. Finally, and this is the core of this work, we investigate in *Section 5* the problem of three interacting spheres, firstly presented by Ramachandran et al. (1989) for heat transfer without diffusion and chemical reaction inside the spheres, with mass transfer coupled to diffusion and chemical

reaction inside the spheres. We test our reactive Sherwood number correlation on this configuration. The validity of the model and the steps forward in extending/improving our reactive Sherwood number correlation are discussed in *Section 6*.

2. Governing equations

We aim at solving the time-dependent and incompressible flow of a Newtonian fluid past multiple fixed obstacles with mass transfer between the fluid and the solid obstacles. We define the full flow domain as Ω, the part of Ω occupied by the solid obstacles as P and the part of Ω occupied by the fluid as $\Omega \backslash P$. The problem is governed by the following conservation equations: fluid mass conservation, fluid momentum conservation and chemical species conservation. Here we assume a single chemical species C at a low concentration in the fluid such that it does not affect the constant density and viscosity of the fluid. Dimensional quantities are distinguished from dimensionless quantities by a "*" superscript. We denote $\boldsymbol{u}^*$ the fluid velocity, p^* the fluid pressure, C_f^* the chemical species concentration in the fluid and C_s^* the chemical species concentration in the solid. The chemical species is assumed to undergo a first order reaction in the solid obstacles. With appropriate initial conditions in Ω on $(\boldsymbol{u}^*, C_f^*, C_s^*)$ and boundary conditions on $\partial\Omega$, the boundary of Ω, on $\boldsymbol{u}^*$ (and potentially on p^*), the set of conservation equations together with fluid/solid interface conditions is written as follows:

- in the fluid

$$\rho_f^* \left(\frac{\partial \boldsymbol{u}^*}{\partial t^*} + (\boldsymbol{u}^* \cdot \nabla)\boldsymbol{u}^* \right) - \eta^* \nabla^2 \boldsymbol{u}^* + \nabla p^* = \boldsymbol{0}, \tag{1}$$

$$\nabla \cdot \boldsymbol{u}^* = 0, \tag{2}$$

$$\frac{\partial C_f^*}{\partial t^*} + \boldsymbol{u}^* \cdot \nabla C_f^* - \nabla \cdot (D_f^* \nabla C_f^*) = 0, \tag{3}$$

  where ρ_f^* denotes the fluid density, η^* the fluid viscosity and D_f^* the chemical species diffusion coefficient in the fluid.

- in the solid

$$\boldsymbol{u}^* = 0, \tag{4}$$

$$\frac{\partial C_s^*}{\partial t^*} - \nabla \cdot (D_s^* \nabla C_s^*) = -k_s^* C_s^*, \tag{5}$$

  where D_s^* denotes chemical species effective diffusion coefficient in the solid and k_s^* the effective first order reaction constant in the solid.

- at the fluid/solid interface ∂P

$$\boldsymbol{u}^* = 0, \tag{6}$$

$$C_s^* = C_f^*, \tag{7}$$

$$-D_s^* \frac{\partial C_s^*}{\partial \boldsymbol{n}} = -D_f^* \frac{\partial C_f^*}{\partial \boldsymbol{n}}, \tag{8}$$

  where $\boldsymbol{n}$ denotes the unit normal vector at the fluid/solid interface.

Governing equations are made dimensionless by introducing a characteristic length L_c^*, a characteristic velocity U_c^* and a characteristic convective time $T_c^* = L_c^*/U_c^*$. In the various problems examined thereafter, solid obstacles are spheres, hence an obvious choice for L_c^* is the particle diameter d_p^*. When the problem is not purely diffusive, an obvious choice for U_c^* is the far field inlet velocity U_{in}^*. Also, by normalizing the chemical species concentration between 0 and 1 and introducing the chemical species diffusion coefficient ratio $\gamma = \frac{D_s^*}{D_f^*}$, conservation equations (3) and (5) together with interface conditions (7)-(8), i.e., continuity of chemical species concentration and continuity of chemical species normal flux, can be recast into a single dimensionless conservation equation for the chemical species C with appropriate no jump conditions at the fluid/solid interface on the chemical species concentration and on its normal flux.

The set of dimensionless equations eventually reads as follows:

$$\frac{\partial \boldsymbol{u}}{\partial t} + (\boldsymbol{u}\cdot\nabla)\boldsymbol{u} - \frac{1}{Re}\nabla^2\boldsymbol{u} + \nabla p = \boldsymbol{0} \quad \text{in} \quad \Omega\backslash P, \tag{9}$$

$$\nabla\cdot\boldsymbol{u} = 0 \quad \text{in} \quad \Omega\backslash P, \tag{10}$$

$$\boldsymbol{u} = \boldsymbol{0} \quad \text{in} \quad P\cup\partial P, \tag{11}$$

$$\begin{aligned} &\frac{\partial C}{\partial t} + \boldsymbol{u}\cdot\nabla C - \nabla\cdot\left(\frac{h(\gamma)}{Pe}\nabla C\right) + \frac{h(\gamma)g(\phi^2)}{Pe}C = 0 \quad \text{in} \quad \Omega, \\ &[C]_{\partial P} = 0 \quad , \quad \left[h(\gamma)\frac{\partial C}{\partial \boldsymbol{n}}\right]_{\partial P} = 0, \end{aligned} \tag{12}$$

where $[\,]_{\partial P}$ represents the jump condition across the fluid/solid interface. The dimensionless numbers introduced above are defined as follows:

- Reynolds number: $Re = \dfrac{\rho_f^* U_c^* L_c^*}{\eta^*}$,
- Peclet number: $Pe = \dfrac{U_c^* L_c^*}{D_f^*}$,
- Damkohler number: $Da = \phi^2 = \dfrac{k_s^* L_c^{*2}}{D_s^*}$

where $\phi = \sqrt{Da}$ is the Thiele modulus, and the functions $h(\gamma)$ and $g(\phi^2)$ are simple Heavyside-like functions defined as:

$$h(\gamma) = \begin{cases} 1 & \text{in} \quad \Omega\backslash P, \\ \gamma & \text{in} \quad P. \end{cases}$$

$$g(\phi^2) = \begin{cases} 0 & \text{in} \quad \Omega\backslash P, \\ \phi^2 & \text{in} \quad P. \end{cases}$$

As usual, we can also introduce a Schmidt number $Sc = \dfrac{\eta^*}{\rho_f^* D_f^*}$ such that $Pe = Re\cdot Sc$. Hence the flow is equivalently characterized by the pair (Re, Pe) or the pair (Re, Sc).

3. Numerical Model

The chemical species problem is one-way coupled only to the fluid problem through the velocity field $\boldsymbol{u}$. At each discrete time t^{n+1}, $n > 0$ being the time index and t^0

being the initial time, we solve the full problem as a sequence of the fluid problem followed by the chemical species problem using the computed velocity field $\boldsymbol{u}^{n+1}$. The solution algorithm is hence of the 1st order in time weak coupling type. In the next subsections, we shortly elaborate on the strategy adopted to solve each sub-problem.

3.1. Solution to the fluid problem: flow around fixed obstacles

We use our well validated Finite Volume/Staggered Grid-DLM/FD solver implemented in our in-house code PeliGRIFF. The whole method is fully detailed in Wachs et al. (2015); Rahmani and Wachs (2014) for freely moving particles and in Dorai et al. (2015) for fixed obstacles and was pionneered by Glowinski et al. (1999) in a Finite Element context. To summarize, we use a cartesian structured mesh of constant grid size around obstacles, we solve the fluid conservation equations (9)-(10) everywhere in the domain (not only in $\Omega \backslash P$ but in the entire Ω) and we enforce the rigid body motion (motionless in the particular case of the application treated in this paper) in the region (filled with fictitious fluid) occupied by the obstacles and represented by (11) using a distributed Lagrange multiplier field. Our Finite Volume/Staggered Grid-DLM/FD method also involves an implicit solution of the resulting DLM/FD saddle-point problem by a Uzawa algorithm, a collocation-point method to discretize the solid obstacles on the fluid mesh and a second-order interpolation of the fluid velocity at the particle boundary (Wachs et al., 2015; Rahmani and Wachs, 2014; Dorai et al., 2015). In our Finite Volume/Staggered Grid discretization method, the diffusive term is discretized with a 2nd order accurate centered scheme while the advective term is discretized with a 2nd order accurate TVD (Total Variation Diminishing)/Superbee limiter scheme. Finally, the diffusive term is treated implicitly in time with a 2nd order Crank-Nicholson scheme while the advective term is treated explicitly in time with a 2nd order Adams-Bashforth scheme. The strength of our method is that it does not require any kind of hydrodynamic radius calibration (see Wachs et al. (2015) for more detail about the problem of hydrodynamic radius calibration). The overall spatial accuracy of the discretization scheme is however not fully 2nd order due to the non-boundary fitted feature of the mesh around the solid obstacles. The dimensionless mesh size Δx is related to the number of points per sphere diameter through $N_p = 1/\Delta x$.

The solution algorithm for the fluid problem is of the 1st order operator-splitting type and comprises two stages as follows:

1. A classical L2-projection scheme for the solution of the Navier & Stokes problem: find $\boldsymbol{u}^{n+1/2}$ and p^{n+1} such that

$$\begin{aligned}\frac{\tilde{\boldsymbol{u}}-\boldsymbol{u}^n}{\Delta t}-\frac{1}{2Re}\nabla^2\tilde{\boldsymbol{u}} &= -\nabla p^{n+1}+\frac{1}{2Re}\nabla^2\boldsymbol{u}^n \\ &\quad -\frac{1}{2}\left(3\boldsymbol{u}^n\cdot\nabla\boldsymbol{u}^n-\boldsymbol{u}^{n-1}\cdot\nabla\boldsymbol{u}^{n-1}\right)-\boldsymbol{\lambda}^n,\end{aligned} \tag{13}$$

$$\nabla^2\psi=\frac{1}{\Delta t}\nabla\cdot\tilde{\boldsymbol{u}}\ ,\ \ \frac{\partial\psi}{\partial n}=0 \text{ or } \psi=0 \text{ on } \partial\Omega, \tag{14}$$

$$\begin{aligned}\boldsymbol{u}^{n+1/2} &= \tilde{\boldsymbol{u}}-\Delta t\nabla\psi, \\ p^{n+1} &= p^n+\psi-\frac{\Delta t}{2Re}\nabla^2\psi.\end{aligned} \tag{15}$$

2. A fictitious domain problem: find $\boldsymbol{u}^{n+1}$ and $\boldsymbol{\lambda}^{n+1}$ such that

$$\frac{\boldsymbol{u}^{n+1}-\boldsymbol{u}^{n+1/2}}{\Delta t}+\boldsymbol{\lambda}^{n+1}=\boldsymbol{\lambda}^n, \tag{16}$$

$$\boldsymbol{u}^{n+1}=\boldsymbol{0}\ \ in\ P. \tag{17}$$

where $\tilde{\boldsymbol{u}}$, $\boldsymbol{\lambda}$, ψ and Δt denote the non divergence-free predicted fluid velocity vector, DLM/FD Lagrange multiplier to relax the constraint (17), pseudo-pressure field and time step, respectively.

3.2. Solution to the chemical species problem: Sharp Interface method

The conservation equation in problem (12) is discretized in time with a 1st order scheme. The diffusive term is treated implicitly in time with a 1st order Backward Euler scheme and the advective term is discretized explicitly in time with a 2nd order Adams-Bashforth scheme. Since the reactive term is linear with C, it can be easily treated implicitly too. The discrete in time version of the conservation equation in problem (12) reads as follows:

$$\begin{aligned}\frac{C^{n+1}-C^n}{\Delta t}-\nabla\cdot\left(\frac{h(\gamma)}{Pe}\nabla C^{n+1}\right)+\frac{h(\gamma)g(\phi^2)}{Pe}C^{n+1} &= \\ -\frac{1}{2}\left(3\boldsymbol{u}^{n+1}\cdot\nabla C^n-\boldsymbol{u}^n\cdot\nabla C^{n-1}\right)&\end{aligned} \tag{18}$$

The primary difficulty in the spatial discretization of (18) is how to discretize the diffusive operator on a non-boundary fitted mesh and to account for the continuity of C and of its normal flux across the fluid/solid interface through the 2 no jump conditions $[C]_{\partial P} = 0$ and $\left[h(\gamma)\frac{\partial C}{\partial \boldsymbol{n}}\right]_{\partial P} = 0$, respectively. This is achieved with a Sharp Interface Method (Fedkiw et al., 1999; Liu et al., 2000; Shao et al., 2012). We use the original version suggested by Fedkiw et al. (1999). The method is only 1st order accurate in space but is discontinuity capturing and easy to implement. The core of the method is to incorporate the jump conditions into the discrete in space diffusive term. The other terms in (18) are discretized in a classical way. Since the method is well established, we simply shortly summarized its construction in 1D and the extension to 3D suggested by Shao et al. (2012) in the special case of spherical solid bodies.

3.2.1. Description of the Sharp Interface Method in one dimension

To ease notation, let's rewrite $\frac{h(\gamma)}{Pe}$ as β. β is hence a diffusion coefficient with a discontinuity across the fluid/solid interface. We shortly elaborate below on the discretization of the diffusive term $\nabla \cdot (\beta \nabla C)$ in 1D, i.e., $(\beta C_x)_x$, with $_x = \frac{\partial}{\partial x}$.

We consider general jump conditions on C and on its flux defined at the interface ∂P as:

$$\left[C\right]_{\partial P} = C^+_{\partial P} - C^-_{\partial P} = a_{\partial P} \tag{19}$$

$$\left[\beta C_x\right]_{\partial P} = \left(\beta C_x\right)^+_{\partial P} - \left(\beta C_x\right)^-_{\partial P} = b_{\partial P} \tag{20}$$

where Ω^- denotes the part of the domain on one side of the interface (e.g., $\Omega^- = \Omega \backslash P$ is the fluid domain) and Ω^+ denotes the part of the domain on the other side of the interface (e.g., $\Omega^+ = P$ is the solid domain). We assume that the 1D space is discretized uniformly with a constant grid size Δx and that the interface ∂P lies between two grid points $i \in \Omega^-$ and $i+1 \in \Omega^+$. Following Fedkiw et al. (1999); Liu et al. (2000), the diffusive term $(\beta C_x)_x$ for point i is discretized in a Finite Difference fashion as follows:

$$\left(\beta C_x\right)_x = \frac{1}{\Delta x}\left[\hat{\beta}\left(\frac{C_{i+1} - C_i}{\Delta x}\right) - \beta^-\left(\frac{C_i - C_{i-1}}{\Delta x}\right)\right] - \frac{\hat{\beta} a_{\partial P}}{\Delta x^2} - \frac{\hat{\beta} b_{\partial P}(1-\zeta)}{\beta^+ \Delta x} \tag{21}$$

where the coefficient $\hat{\beta}$ is calculated as follows:

$$\hat{\beta} = \frac{\beta^+ \beta^-}{\beta^+ \zeta + \beta^- (1 - \zeta)} \tag{22}$$

and ζ is the cell fraction, calculated through the level set function χ based on the interface location.

$$\zeta = \frac{|\chi_i|}{|\chi_i| + |\chi_{i+1}|} \tag{23}$$

In our case, we have neither a jump for C nor for its flux βC_x, which translates into $a_{\partial P} = 0$ and $b_{\partial P} = 0$, so (21) simplifies to:

$$\left(\beta C_x\right)_x = \frac{1}{\Delta x}\left[\hat{\beta}\left(\frac{C_{i+1} - C_i}{\Delta x}\right) - \beta^-\left(\frac{C_i - C_{i-1}}{\Delta x}\right)\right] \tag{24}$$

3.2.2. Extension to three dimensions

The discretization of the diffusive term $\nabla \cdot (\beta \nabla C)$ in the vicinity of an interface ∂P in 3D is a bit trickier as jump conditions exist only for C and its normal flux $[\beta C_n]_{\partial P} = 0$, but nothing is specified about the tangential flux across ∂P. Liu et al. (2000) suggested a dimension by dimension application of the 1D discretization method that we adopt here. However, Liu et al. (2000) also emphasized that a simple projection of the normal flux jump condition on the cartesian coordinate axis leads to the right jump condition in the normal direction but also imposes an artificial and essentially physically wrong additional condition on the tangential flux across ∂P of the form $[\beta C_t]_{\partial P} = 0$, while the right physical condition is simply $[C_t]_{\partial P} = 0$.

Since our solid obstacles are all spheres, we follow the approach suggested by Shao et al. (2012) that involves changing coordinates from cartesian to spherical and writing the jump conditions in cartesian coordinates as a function of the jump conditions in spherical coordinates in a way that the right jump conditions are imposed.

Cartesian and spherical coordinate systems are related to each other through:

$$x = r\sin(\theta)\cos(\varphi) \tag{25}$$

$$y = r\sin(\theta)\sin(\varphi) \tag{26}$$

$$z = r\cos(\theta) \tag{27}$$

with $\theta \in [0, 2\pi]$ and $\varphi \in [-\pi/2, +\pi/2]$. The gradient of C in the cartesian coordinate system is related to the gradient of C in the spherical coordinate system through:

$$C_x = C_r \sin(\theta)\cos(\varphi) + C_{t_\theta}\cos(\theta)\cos(\varphi) - C_{t_\varphi}\sin(\varphi) \tag{28}$$

$$C_y = C_r \sin(\theta)\sin(\varphi) + C_{t_\theta}\cos(\theta)\sin(\varphi) + C_{t_\varphi}\cos(\theta) \tag{29}$$

$$C_z = C_r \cos(\varphi) - C_{t_\varphi}\sin(\varphi) \tag{30}$$

where t_θ is the unit tangential vector in the θ direction and t_φ is the unit tangential vector in the φ direction. Obviously on a sphere surface we have $C_r = C_n$. Multiplying the above equations by β we can write the jump conditions in the cartesian directions x, y and z as a function of the jump conditions in the normal and tangential directions as:

$$\begin{aligned}[\beta C_x]_{\partial P} = [\beta C_n]_{\partial P}\sin(\theta)\cos(\varphi) + [\beta C_{t_\theta}]_{\partial P}\cos(\theta)\cos(\varphi) \\ - [\beta C_{t_\varphi}]_{\partial P}\sin(\theta)\end{aligned} \tag{31}$$

$$\begin{aligned}[\beta C_y]_{\partial P} = [\beta C_n]_{\partial P}\sin(\theta)\sin(\varphi) + [\beta C_{t_\theta}]_{\partial P}\cos(\theta)\sin(\varphi) \\ + [\beta C_{t_\varphi}]_{\partial P}\cos(\theta)\end{aligned} \tag{32}$$

$$[\beta C_z]_{\partial P} = [\beta C_n]_{\partial P}\cos(\varphi) - [\beta C_{t_\theta}]_{\partial P}\sin(\varphi) \tag{33}$$

In our problem, we have $[C]_{\partial P} = 0$, $[\beta C_n]_{\partial P} = 0$, $[C_{t_\theta}] = 0$ and $[C_{t_\varphi}] = 0$. However, $[\beta C_{t_\theta}]_{\partial P} = [\beta]_{\partial P} C_{t_\theta}$ and $[\beta C_{t_\varphi}]_{\partial P} = [\beta]_{\partial P} C_{t_\varphi}$ are non zero because $[\beta]_{\partial P} \neq 0$, i.e., the diffusion coefficient β is discontinuous across the interface ∂P. To calculate these 2 terms, we need to calculate the tangential derivatives C_{t_θ} and C_{t_φ} at the particle surface. At the discrete level, these 2 tangential derivatives are approximated for each point on the particle surface using a central difference scheme that involves the values of C at two adjacent points. As C is not known at the time level t^{n+1}, we use C from the previous time level, i.e., t^n, to compute C_{t_θ} and C_{t_φ} as suggested by Shao et al. (2012). Eventually, the 3 jump conditions (31)-(33) are added to the right hand side of the conservation equation as in a 1D case.

4. Validations

We verify here our implementation of the SIM and assess its capability to resolve the different flow problems we are interested in. We perform a step by step validation of the computed solution in problems of growing complexity. For diffusion and diffusion-reaction problems, we compare our SIM results to existing analytical solutions. For convection-diffusion problems, we compare our SIM results to existing correlations. Finally, for convection-diffusion-reaction problems, there does not exist any correlation or analytical solution, to the best of our knowledge. For this reason, we compare our SIM results to results computed with a boundary-fitted method with local mesh refinement that fully resolves the gradients at the particle interface. We test the limitations of SIM for a wide range of dimensionless numbers. In all the cases examined from now on, we are interested in the steady state solution only. However, the steady state solution is computed by our transient algorithm as the solution obtained when time derivatives are negligibly small. All transient computations are run with $\Delta t = 10^{-3}$.

4.1. Pure diffusion in a finite domain

4.1.1. Steady state diffusion from a single particle

The first validation test is performed in a purely diffusive regime. A spherical particle of radius r_p^* is placed at the center of a cubic domain $\Omega = L_x^* \times L_y^* \times L_z^*$ and a zero concentration $C_s = 0$ is imposed at the particle boundary and inside the particle. This condition is enforced through an infinitely fast reaction $\phi^2 \to \infty$ and a large diffusion coefficient ratio γ that makes the problem mass transfer controlled. A fixed concentration C_∞ is imposed at the boundary $\partial\Omega$ of the domain so that the concentration difference (or driving force) is constant. When the problem is posed in a spherical domain Ω of finite radius r_∞^*, we can solve the 1D problem and derive an expression for the Sherwood number (see Appendix A for the details) as follows:

$$Sh = \frac{k^* d_p^*}{D_f^*} = \frac{2r_\infty^*}{r_\infty^* - r_p^*} \tag{34}$$

where k^* denotes the mass transfer coefficient defined as:

$$k^* = \frac{D_f^*}{4\pi r_p^{*2}(C_\infty - C_s)} \int_{-\pi/2}^{\pi/2} \int_0^{2\pi} \left. \frac{\partial C(r^*)}{\partial r^*} \right|_{r^*=r_p^*} r_p^{*2} sin(\theta) d\phi d\theta \qquad (35)$$

We set the dimensionless box size to $L_x = L_y = L_z = 10$. The particle dimensionless radius is $r_p = 0.5$. The analytical value of the Sherwood number in a spherical domain of finite radius $r_\infty = 5$ is $Sh_{an} = 20/9 = 2.22$. We assume that this solution is a good approximation of the solution posed in a cubic domain $L_x = L_y = L_z = 2r_\infty$. We examine the convergence of the method by computing Sh as a function of the grid size $\Delta x = 1/N_p$. We then compute the relative error with respect to Sh_{an} as $\epsilon = \frac{Sh(N_p) - Sh_{an}}{Sh_{an}}$ and plot the convergence of ϵ with N_p in FIG. 1. The solution follows an expected first order spatial convergence. In this test, the error originates from two contributions. The first contribution is related to the spatial discretization of the problem and the contribution we are interested in. The second contribution is due to the fact that the analytical solution is derived in a spherical domain and compared to the computed solution in a cubic box. For the range of N_p considered, it is clear in FIG. 1 that the second contribution is negligible and that provided $r_\infty = L_x/2$ is chosen large enough, the analytical solution in a spherical domain does not differ much from the solution in a cubic domain.

4.1.2. Steady state diffusion from a single particle in a gradient of concentration

We test our SIM in another diffusive configuration previously examined by Shao et al. (2012). A solid particle of diffusion coefficient D_s^* is immersed at the center of a cubic domain $\Omega = L_x^* \times L_y^* \times L_z^*$ of fluid at rest of diffusion coefficient D_f^*. Dirichlet boundary conditions $C = C_1 = 1$ at the top wall and $C = C_2 = 0$ at the bottom wall are imposed to generate a concentration gradient in the z direction. Zero normal flux boundary conditions are imposed on the 4 lateral walls. The average Sherwood number corresponding to the flux through a horizontal xy plane is defined as:

$$Sh = \frac{L_z^*}{C_2 - C_1} \cdot \frac{1}{L_x^* L_y^*} \int_0^{L_x^*} \int_0^{L_y^*} \left(\frac{\partial C}{\partial z^*} \right) dy^* dx^* \qquad (36)$$

The average Sherwood number can be analytically predicted based on the analogy

with Maxwell-Garnett electric conductivity (Maxwell et al., 2005) as:

$$Sh = 1 + \frac{3\alpha(\gamma - 1)}{\gamma + 2} \tag{37}$$

where α is the solid volume fraction. Following Shao et al. (2012), we simulate two cases with two different solid volume fractions. We keep the dimensional box size constant to $L_x^* = L_y^* = L_z^* = 10mm$ and vary the solid volume fraction α through selecting 2 different particle radii $r_p^* = 1.25mm$ and $r_p^* = 2mm$, i.e., $r_p^*/L_x^* = 0.125$ and $r_p^*/L_x^* = 0.2$, respectively. We select the diffusion ratio γ to span the interval $[10^{-2}, 10^2]$. For each value of γ we compute the average Sherwood number and compare its value to the theoretical prediction and the numerical results of Shao et al. (2012). FIG. 2 exhibits a very satisfactory agreement of our results with both the analytical prediction and numerical results of Shao et al. (2012). We compute an additional case for $r_p^* = 1.5mm$, i.e., $r_p^*/L_x^* = 0.15$, and plot the convergence towards the analytical solution in FIG. 3 for the three solid volume fractions corresponding to $r_p^*/L_x^* = 0.1, 0.15, 0.2$. As expected, a first order spatial convergence is obtained. The error is shown to increase with the increase of α. The concentration contours in a xz vertical cut plane containing the sphere center are illustrated in FIG. 4 for the case of $r_p^*/L_x^* = 0.2$ and $\gamma = 0.1$.

4.2. Steady state internal diffusion and chemical reaction in a single particle

We consider a spherical porous catalyst particle of diameter d_p^* and diffusion coefficient D_s^* immersed at the center of a cubic domain $\Omega = L_x^* \times L_y^* \times L_z^*$. The particle is assumed to undergo a first order chemical reaction controlled by a constant k_s^* such that the chemical species concentration C inside the particle satisfies (5). If the surface concentration denoted C_s is known and assumed to be constant over the sphere surface, the problem becomes 1D in space and we can easily write the steady state solution of (5) as follows:

$$C(r) = C_s \frac{\sinh(\phi r)}{2r \sinh(\phi/2)} \tag{38}$$

where as usual $r = r^*/d_p^*$ is the dimensionless radial position and $\phi = d_p^* \sqrt{\frac{k_s^*}{D_s^*}}$ is the Thiele modulus. The derivation of (38) can be found in many textbooks.

Dirichlet boundary conditions $C = 1$ are imposed on the 6 walls of the cubic domain. We impose $C_s = 1$ through an infinitely large diffusion coefficient D_f^* in fluid phase, i.e., γ is chosen asymptotically small. The domain size does not matter here and only needs to be chosen dimensionlessly larger than 1. We compare our SIM concentration profile inside the particle to the analytical solution (38) in FIG. 5 for $N_p = 20$. The agreement is once again very satisfactory. The numerical method is capable of capturing the steep concentration gradients at the particle surface even for a modest resolution. The corresponding concentration iso-countours are shown in FIG. 6 for $N_p = 80$.

Based on the concentration profile, the effectiveness factor η for a catalyst particle can be defined as the ratio of the overall internal reaction rate in the particle to the reaction rate that can be attained in the absence of diffusion limitations. For a spherical catalyst particle with a fixed surface concentration C_s, we have:

$$\begin{aligned}\eta &= \frac{\int_0^{2\pi}\int_{-\pi/2}^{+\pi/2}\int_0^{r_p^*} -k_s^* C(r^*) sin(\theta) r^{*2} d\phi d\theta dr^*}{-k_s^* \frac{4\pi}{3} r_p^{*3} C_s} \\ &= \frac{\overline{C_v}}{C_s} = \frac{3}{\phi}\left(\frac{1}{tanh(\phi)} - \frac{1}{\phi}\right)\end{aligned} \tag{39}$$

where $C(r^*) = C_s \dfrac{r_p^* \sinh(\phi r^*)}{r^* \sinh(\phi r_p^*)}$ is the Thiele concentration profile given by (38) in a dimensional form for a given surface concentration C_s and $\overline{C_v}$ is the average volume concentration in the particle.

Depending on reaction kinetics and assuming, e.g., $\gamma \in [10^{-2}, 10^2]$, i.e., γ is not asymptotically small/large, the effectiveness factor η exhibits two asymptotic limits. When the reaction rate is very low compared to diffusion, $\phi \ll 1$, the system is controlled by kinetics and the catalyst surface concentration C_s is equal to fluid concentration, and so $\eta \to 1$. When the reaction rate is high compared to diffusion, i.e. $\phi \gg 1$, the system is limited by diffusion and the surface concentration C_s approaches zero, therefore $\eta \to 3/\phi$.

In the following test, we once again impose $C_s = 1$ through an asymptotically small γ. We vary the Thiele modulus ϕ in the range $[0.2, 120]$ by varying the reaction

rate constant k_s^*. For each value of ϕ, we calculate numerically the effectiveness factor η and examine the spatial convergence of the solution computed with our SIM and a standard VOF method. Hence we compute SIM solutions for $N_p = 10, 40, 80$ and VOF solutions for $N_p = 40, 80$. FIG. 7 shows η as a function of ϕ for $N_p = 10, 80$ with SIM and $N_p = 40$ with VOF. Results obtained with SIM and VOF are further compared to each other and to the analytical solution in FIG. 8 and FIG. 9 for various values of ϕ and N_p. We can make the 3 following comments: (ii) both methods show a first order spatial convergence, (ii) VOF with a grid size 4 times smaller than SIM gives approximately the same computed solution, and (iii) when $N_p = 80$, SIM predictions are very close to the analytical solution with a slightly growing deviation for $\phi > 20$. The superior accuracy of the solution computed with SIM compared to that computed with VOF is further emphasized in FIG. 8 where we plot the error to the analytical solution as a function of ϕ for $N_p = 80$. Finally, FIG. 9 also highlights that fact that the magnitude of the error increases with increasing ϕ in relation to the concentration gradients becoming steeper in the vicinity of the particle surface as ϕ increases, i.e., the internal mass boundary layer gets thinner as ϕ increases.

4.3. Steady state convection-diffusion in the flow past a single sphere: external mass transfer problem

We now validate our SIM in the case of external mass transfer in the flow past a spherical solid particle in an unbounded domain. A spherical particle is placed in a box of size $L_x \times L_y \times L_z = 5 \times 5 \times 15$. The fluid enters the flow domain on the left boundary with an imposed fluid velocity $\mathbf{u} = (0, 0, 1)$ and a concentration $C = C_\infty = 1$. The particle is centered in the x and y directions. Periodic boundary conditions are imposed in x and y directions and $C = C_\infty = 1$ is imposed on the 4 lateral walls while a classical outflow boundary condition $\frac{\partial \mathbf{u}}{\partial z} = \frac{\partial C}{\partial z} = 0$ and $p = p_{ref} = 0$ is imposed at the outlet boundary. FIG. 10 illustrates the flow configuration in a xz cut plane containing the sphere center. The concentration C in the particle is imposed to 0 by selecting an extremely large value of ϕ. The problem is hence controlled by Sc and Re.

To illustrate that our SIM predicts the right external mass transfer, we set $Sc = 1$

and vary Re in the range $[0, 200]$. We compute the steady state Sherwood number Sh for $N_p = 80$ and compare its value to literature correlations as, e.g., the correlation of Feng and Michaelides (2000), in FIG. 11. Overall, we observe a very satisfactory agreement between our SIM results and literature correlations.

4.4. Steady state convection-diffusion in the flow past a single reactive sphere: external-internal mass transfer

We now consider a similar problem to the one in *Section 4.3* but with a first order reaction inside the particle. To validate our SIM, we compare the results computed with our SIM to results supplied by a highly accurate boundary fitted method implemented in the JADIM code. JADIM solves the same system of equations (9)-(12) but with a different discretization scheme in space and in time. The high accuracy of solutions computed with JADIM derives both from its boundary fitted spatial discretization scheme and the ability to locally refine the mesh in both the internal and external mass boundary layers.

The numerical methods used in JADIM have been thoroughly described by Magnaudet et al. (1995) and Calmet and Magnaudet (1997). Consequently they are only quickly summarized here. The JADIM code solves the incompressible Navier-Stokes equations and the concentration equation in general orthogonal curvilinear coordinates which are boundary fitted to the particle surface. Equations are integrated in space using a finite volume method in which advective and diffusive terms are evaluated with second-order accurate centered schemes. The solution is advanced in time by means of a three-step Runge-Kutta time-stepping procedure in which advective terms are computed explicitly while diffusive terms are treated by a semi-implicit Crank-Nicholson scheme. Incompressibility is satisfied after the third intermediate time step by solving a Poisson equation for an auxiliary potential from which the true pressure is deduced, similarly to (13)-(15). The complete algorithm is second order accurate in both space and time.

The mesh grid used in the present work is sketched in FIG. 12. The orthogonal axisymmetric mapping is obtained by using the streamlines and the equipotential lines of the potential flow around a circular cylinder. The mesh is stretched in order to have at

least four points in the external mass boundary layer that scales as $Pe^{-1/3}$. Simulations are performed in a 2D axisymmetric configuration which reproduces the geometry of a spherical particle. The fluid computational domain is limited by the particle surface and by external boundaries on which inflow, free stream, axial symmetry, and outflow boundary conditions are imposed. The equations are solved inside the particle over a polar mesh adjusted to the fluid mesh at the particle surface. The internal mass boundary layer thickness reduces when the kinetics of the chemical reaction, i.e., ϕ, increases. The mesh inside the particle is thus refined close to the particle surface following the scaling of the boundary layer as ϕ^{-1}. At least four grid points stand within the internal boundary layer in order to compute properly the internal concentration gradient at the particle surface. A particle of radius r_p^* is placed in a domain with a spatial extension of at least $r_\infty^* = 100 r_p^*$, so that the assumption of infinite domain is physically valid.

All simulations are performed with $N_p = 80$ unless spatial convergence is investigated. The used DLM-FD simulation domain is $5 \times 5 \times 15$. We set $\gamma = 10$, $\phi = 2$ and $Sc = 1$ and vary Re in the range $[0, 200]$. Our SIM results plotted in FIG. 13 agree well with the JADIM results and the model for the mean surface concentration $\overline{C_s}$ suggested in Sulaiman et al. (2018). FIG. 13 shows that the mean surface concentration $\overline{C_s}$ increases with the increase of Re. Then we set $\gamma = 10$, $\phi = 150$ and $Sc = 1$ and vary ϕ in the range $[0, 40]$. Once again a good agreement between our SIM results, the JADIM results and the model for the mean surface concentration $\overline{C_s}$ suggested in Sulaiman et al. (2018) is highlighted in FIG. 14, with a small deviation of our SIM results from the JADIM results and the model predictions that grows as ϕ increases due to the internal boundary layer getting thinner as $1/\phi$.

We now compare concentration profiles computed with our SIM and JADIM. We set $\gamma = 10, Re = 10$, and $Sc = 1$, select two Thiele moduli $\phi = 4$ and $\phi = 10$ and plot the concentration profile obtained with each method in FIG. 15. The agreement is visually very good. The actual error between SIM and JADIM (not shown here for the sake of conciseness) increases for $\phi = 10$ compared to $\phi = 4$, in line with what we observe for $\overline{C_s}$. We run another set of simulations with $\gamma = 10$, $\phi = 10$, $Sc = 1$ and two Reynolds numbers $Re = 10$ and $Re = 100$. Concentration profiles plotted in FIG. 16 once again in a cross-section normal to the inlet flow, corresponding

to $\theta = 90$. They highlight a satisfactory agreement between our SIM results and the JADIM results. The error between SIM and JADIM (not shown here for the sake of conciseness) only mildly increases with Re. The numerical accuracy is consequently mostly controlled by the internal mass boundary layer thickness.

Finally, we examine the spatial convergence of the SIM computed solution to the JADIM reference solution. We set $\gamma = 0.1$, $\phi^2 = 40$ and $Re = 150$, select $Sc = 0.1$, $Sc = 1$ and $Sc = 10$ and N_p in the range $[10, 80]$. We then compute and plot the error ϵ on the mean surface concentration $\overline{C_s}$ between SIM and JADIM. FIG. 17 shows that ϵ increases slightly only with the increase of Sc. This behavior is similar to the behavior of the solution with increasing Re at constant ϕ, that shows that ϵ is mainly controlled by the reaction rate and the internal mass boundary layer thickness. To investigate the effect of the reaction rate on the solution, we perform a final set of simulations with $\gamma = 0.1$, $Sc = 10$, $Re = 150$ and ϕ^2 varying in the range $[40, 4000]$. FIG. 18 reveals that ϵ increases significantly with the increase of ϕ^2. For $\phi^2 = 40$, even a mesh resolution $N_p = 20$ is sufficient to supply a computed solution with a relative error of 3%. At $\phi^2 = 200$, a grid resolution $N_p = 60$ is needed to reach the same accuracy. For $\phi^2 = 400$, a grid resolution with more than $N_p = 80$ is needed to reach an accuracy corresponding to a relative error of less than 4%. And finally at $\phi^2 = 4000$, even the finest grid resolution considered here $N_p = 80$ supplies a computed solution that is still 11% off from the reference solution.

5. Interacting Spheres

We examine here the external forced convection-diffusion on a sequence of interacting spheres undergoing an internal first order irreversible chemical reaction. The non-reactive problem without diffusion inside solid bodies was firstly introduced by (Ramachandran et al., 1989) for heat transfer. As in *Section 4*, we are interested in the steady state solution only and all transient computations leading to steady state are run with $\Delta t = 10^{-3}$. Ramachandran et al. (1989) suggested empirical corrective terms to relate the non-reactive Sherwood number of a single sphere to the non-reactive Sherwood numbers of interacting spheres. The corrective terms account for separation

distances effect between the particles. The aim of this work is to include the effect of a chemical reaction inside the solid bodies and to introduce, based on internal-external coupling, a model for the reactive Sherwood number for each particle, that accounts for the effects of diffusion, convection, and reaction. We aim at extending the model we suggested for a single sphere in (Sulaiman et al., 2018) to more concentrated particle-laden flows and consider the flow configuration investigated here as a proper toy model for mass transfer with reaction in dilute particle-laden flows. The core aspect of our model is that it is possible to construct a reactive Sherwood number formula based on an existing non-reactive Sherwood number formula. We show thereafter that this approach is still valid in dilute particle-laden systems experiencing hydrodynamic interactions.

5.1. Problem definition

We consider a system composed of three aligned spherical catalyst particles along z in a box of size $L_x \times L_y \times L_z = 5 \times 5 \times 15$. The fluid enters the flow domain on the left boundary with an imposed fluid velocity $\mathbf{u} = (0, 0, 1)$ and concentration $C = 1$. The three particles are centered in the x and y directions. Periodic boundary conditions are imposed in x and y directions and $C = C_\infty = 1$ is imposed on the 4 lateral walls while a classical outflow boundary condition $\frac{\partial \mathbf{u}}{\partial z} = \frac{\partial C}{\partial z} = 0$ and $p = p_{ref} = 0$ is imposed at the outlet boundary. The separation distances between the first and second particles and between the second and third particles are d_{12} and d_{23}, respectively, as shown in FIG. 19. The problem is controlled by the Reynolds number Re, the Schmidt number Sc, the diffusion coefficient ratio γ and the Damkohler ϕ^2. All computations are performed with $N_p = 70$.

We approach the problem through the external-internal coupling based on the continuity of C and of its normal flux at the fluid/solid interface ∂P. The normal flux density at the particle surface in the solid phase $N^*_{s,\partial P}$ is given by:

$$N^*_{s,\partial P} = -D^*_s \frac{dC}{dr^*}\bigg|_{r^*=r^*_p} \tag{40}$$

The concentration profile in the solid phase is given by (38). Calculating the radial derivative at $r^* = r^*_p$ (or $r = 0.5$), the flux in the solid phase can be written as:

$$N^*_{s,\partial P} = -\frac{D^*_s C_s}{r^*_p}\left(\frac{\phi}{tanh(\phi)} - 1\right) \tag{41}$$

The normal flux density at the particle surface in the fluid phase $N^*_{f,\partial P}$ can be written as:

$$N^*_{f,\partial P} = -k^*_f(C_s - C_\infty) \tag{42}$$

where k^*_f is the external mass transfer coefficient in the fluid phase, analytically unknown in case of external convection. The continuity of the normal flux at ∂P, i.e., $N^*_{s,\partial P} = N^*_{f,\partial P}$, leads to:

$$k^*_f(C_s - C_\infty) = D^*_s \frac{C_s}{r^*_p}\left(\frac{\phi}{tanh(\phi)} - 1\right) \tag{43}$$

And we can hence deduce the expression of the surface concentration C_s:

$$C_s = \frac{C_\infty}{1 + \frac{D^*_s}{r^*_p k^*_f}(\frac{\phi}{tanh(\phi)} - 1)} \tag{44}$$

In order to determine C_s, we need to evaluate the external mass transfer coefficient k^*_f. Here, we assume that the internal problem is only affecting the external problem through the concentration gradient. Thus, the external Sherwood number is assumed independent of the reaction rate. We hence evaluate the external mass transfer coefficient from the external Sherwood number Sh, i.e., a non-reactive Sherwood number, as $k^*_f = Sh\, D^*_f/d^*_p$. Then, any appropriate empirical correlation available in the literature for Sh can be used. For instance in (Sulaiman et al., 2018), we used for a single sphere the correlation defined by Feng and Michaelides (2000):

$$Sh = 0.992 + Re^{1/3}Sc^{1/3} + 0.1Re^{2/3}Sc^{1/3} \tag{45}$$

For a series of three interacting spheres, Ramachandran et al. (1989) suggested to account for the interactions between the spheres through corrective coefficients for the Sherwood number of each of the three spheres. These corrective coefficients, mainly empirical, are established based on computational data, and related to the correlation for a single sphere. The individual Sherwood number reads:

$$Sh_j = Sh \cdot \beta_j \quad j = 1, 2, 3 \tag{46}$$

where j is the sphere number and the β_j , $j = 1, 2, 3$ are the empirical corrective terms defined by Ramachandran et al. (1989) as:

$$\beta_1 = 0.9555 Sc^{0.0276} Re^{0.0108} d_{12}^{0.113/[1+1.5ln(10Pe)]} e^{-0.02113/d_{23}} \tag{47}$$

$$\beta_2 = 1 - 0.0697(1 + ln(Re))^{0.767}[1 + ln(10ReSc)]^{0.095} {d_{23}}^{-0.13} - 4.807(1 + ln(Re))^{0.012} d_{12}^{-5.28} \tag{48}$$

$$\beta_3 = 1 - 0.532 Sc^{-0.019} Re^{0.032} e^{-0.0146/d_{12}} \left(\frac{1}{d_{23}}\right)^{3.044/[1+1.1ln(10Pe)]} \tag{49}$$

The average surface concentration $\overline{C_{s,j}}$ for sphere j with corresponding Sherwood number Sh_j, can be written as follows:

$$\overline{C_{s,j}} = \frac{C_\infty}{1 + \frac{2\gamma}{Sh_j}(\frac{\phi}{tanh(\phi)} - 1)} \qquad j = 1, 2, 3 \tag{50}$$

The formulation of a 'reactive' Sherwood number that accounts for convection, diffusion and reaction is based on two concentration gradients instead of a single concentration gradient in the external non-reactive case. The first gradient is the external gradient involving $(\overline{C}_s - C_\infty)$ and the second gradient is the internal gradient involving $(\overline{C_v} - \overline{C_s})$, where $\overline{C_v}$ is the mean volume concentration of C in each sphere. To derive an expression for $\overline{C_v}$, we integrate the 1D concentration profile given by (38), assuming C_s is a function of the position on the sphere and the radial dependence is still reasonably valid, over the particle volume as

$$\overline{C_v} \simeq \frac{3}{4\pi r_p^{*3}} \int_0^{2\pi} \int_{-\pi/2}^{+\pi/2} \int_0^{r_p^*} C_s(\phi, \theta) \frac{r_p^* \sinh(\phi r^*)}{r^* \sinh(\phi r_p^*)} sin(\theta) r^{*2} d\phi d\theta dr^* \tag{51}$$

and further approximate this integral as:

$$\begin{aligned} \overline{C_v} &\simeq \frac{3\overline{C_s}}{4\pi r_p^{*3}} \int_0^{2\pi} \int_{-\pi/2}^{+\pi/2} \int_0^{r_p^*} \frac{r_p^* \sinh(\phi r^*)}{r^* \sinh(\phi r_p^*)} sin(\theta) r^{*2} d\phi d\theta dr^* \\ &= \frac{3\overline{C_s}}{\phi} \left(\frac{1}{tanh(\phi)} - \frac{1}{\phi}\right) \end{aligned} \tag{52}$$

$\overline{C_s}$ is estimated by model (50) and we eventually obtain an expression for the mean volume concentration $\overline{C_{v,j}}$ for sphere j that reads as follows:

$$\overline{C_{v,j}} = \frac{3C_\infty}{1 + \frac{2\gamma}{Sh_j}(\frac{\phi}{tanh(\phi)} - 1)} \left(\frac{1}{\phi tanh(\phi)} - \frac{1}{\phi^2}\right) \qquad j = 1, 2, 3 \tag{53}$$

The conjugate mass transfer problem is formulated with the additivity rule. The additivity rule states that the overall resistance to mass transfer in the system is the sum of two resistances. The resistance is related to the inverse of the mass transfer coefficients. We hence define the 2 Sherwood numbers as:

- internal Sherwood number Sh_{in}

$$Sh_{in} = \frac{N^*_{s,\partial P}\, d^*_p}{D^*_s(\overline{C_s} - \overline{C_v})} = \frac{k^*_{in} d^*_p}{D^*_s} \tag{54}$$

  where k^*_{in} is the internal mass transfer coefficient.

- external Sherwood number Sh

$$Sh = \frac{N^*_{f,\partial P}\, d^*_p}{D^*_f(C_\infty - \overline{C_s})} = \frac{k^*_f d^*_p}{D^*_f} \tag{55}$$

We now introduce the total mass transfer coefficient $\tilde{k}^*$ and write the additivity rule as:

$$\frac{1}{\tilde{k}^*} = \frac{1}{k^*_{in}} + \frac{1}{k^*_f} \tag{56}$$

(56) can be reformulated in terms of Sherwood numbers. Introducing the reactive (i.e. total) Sherwood number $\widetilde{Sh} = \dfrac{\tilde{k}^* d^*_p}{D^*_f}$, we get:

$$\frac{1}{\widetilde{Sh}} = \frac{1}{\gamma Sh_{in}} + \frac{1}{Sh} \tag{57}$$

Finally, using the continuity of the flux density at ∂P, we can obtain Sh_{in} as a function of Sh, inert this in (57) and after some simple algebra get the following expression:

$$\widetilde{Sh} = Sh\frac{C_\infty - \overline{C_s}}{C_\infty - \overline{C_v}} = Sh\frac{\Delta\overline{C_s}}{\Delta\overline{C_v}} \tag{58}$$

with $\Delta\overline{C_s} = C_\infty - \overline{C_v}$ and $\Delta\overline{C_v} = C_\infty - \overline{C_s}$. Finally, using (50) and (52), we establish the expression of the reactive Sherwood number $\widetilde{Sh}$ of each sphere as:

$$\widetilde{Sh_j}(Re, Sc, \phi, \gamma) = \frac{Sh_j(Re, Sc)}{\dfrac{Sh_j(Re, Sc)}{2\gamma}\left[\dfrac{tanh(\phi)}{\phi - tanh(\phi)} - \dfrac{3}{\phi^2}\right] + 1} \qquad j = 1, 2, 3 \tag{59}$$

$Sh_j(Re, Sc)$ in the above expression is the individual Sherwood number for a sphere j in the convective-diffusive problem (without reaction) where the particle internal concentration is uniform, and the mass transfer is only controlled by the Reynolds number Re and the Schmidt number Sc. The 'reactive' Sherwood number, $\widetilde{Sh_j}(Re, Sc, \phi, \gamma)$, also depends on the Damkohler number $Da = \phi^2$ and the diffusion coefficient ratio γ, in addition to the first two dimensionless numbers for convection-diffusion. (59) can further be written in an explicit form:

$$\frac{1}{\widetilde{Sh_j}} = \frac{1}{2\gamma}\left[\frac{tanh(\phi)}{\phi - tanh(\phi)} - \frac{3}{\phi^2}\right] + \frac{1}{Sh_j} \tag{60}$$

(60) has two asymptotic limits. When the reaction rate is very fast, i.e., the Thiele modulus $\phi \to \infty$, the term $\left[\frac{tanh(\phi)}{\phi - tanh(\phi)} - \frac{3}{\phi^2}\right] \to 0$ and so $\widetilde{Sh_j} \to Sh_j$. In this case the system is limited by diffusion, i.e., controlled by mass transfer. When the reaction rate is very slow, i.e. the Thiele modulus $\phi \to 0$, the term $\left[\frac{tanh(\phi)}{\phi - tanh(\phi)} - \frac{3}{\phi^2}\right] \to \infty$, $\widetilde{Sh_j} \to 0$. In this case the system is controlled by internal reaction kinetics.

5.2. Model validation

We examine here how the model performs in the 3-aligned sphere configuration by spanning ranges of the 4 governing dimensionless numbers Re, Sc, γ and ϕ^2, as well as assorted interparticle distances. The mean surface concentration $\overline{C_s}$, given by (50), is the main unknown in the problem. Therefore, we primarily assess the validity of our proposed model by comparing $\overline{C_s}$ as computed by our DLM/FD-SIM numerical method to $\overline{C_s}$ as predicted by our model.

We vary the dimensionless parameters in the ranges: $Re \in [0, 100]$, $\phi^2 \in [0, \infty]$, $Sc \in [0.5, 10]$ and $\gamma \in [10^{-2}, 10^2]$ and select the following three different geometric configurations:

A. $d_{12} = 4$ and $d_{23} = 2$,

B. $d_{12} = 2$ and $d_{23} = 4$,

C. $d_{12} = 2$ and $d_{23} = 2$.

We first examine the influence of the geometric configuration. To do this, we set $Re = 50$, $\gamma = 0.1$, and $Sc = 1$ and keep them constant while we vary the Damkohler

number ϕ^2 in the range $[0, 400]$ and compare our model to our numerical results for the three geometric configurations A, B, and C in FIG. 20, FIG. 21 and FIG. 22, respectively. Overall, $\overline{C_s}$ as predicted by the model show a good agreement with computed $\overline{C_s}$ for the three geometric cases. Essentially, the error increases with the increase of ϕ^2 as the internal concentration boundary layer thickness decreases with the increase of ϕ^2 as $1/\phi$. However, the inter-particle distances have literally no impact on the magnitude of the differences between model predictions and numerical results. Even in configuration C where the 3 particles are the closest to each other, no significant difference is visible between FIG. 22, and FIGS. 20 and 21. For the 3 configurations, the system is still dilute enough such that the first sphere behaves similarly, and quite close to a single isolated sphere.

From now on, we consider the geometric configuration A in the rest of this subsection. We fix $Re = 50$, $Sc = 1$, and $\phi^2 = 40$ and we vary the diffusion ratio γ in the range $[10^{-2}, 10^2]$. Once again, we compute numerically the mean surface concentration $\overline{C_s}$ and we compare it to the value predicted by the model for the three particles in FIG. 23. Results show again a good agreement between model predictions and numerical results.

Finally, we examine the influence of Sc. To do this, we fix $Re = 50$, $\gamma = 0.1$, and $\phi^2 = 40$ and we vary $Sc \in [0.5, 10]$, which consequently varies $Pe \in [25, 500]$. Computed $\overline{C_s}$ is compared to $\overline{C_s}$ predicted by the model for the three particles in FIG. 24. The agreement is deemed to be satisfactory.

We now plot $\overline{C_s}$ as a function of $Re \in [0, 100]$ and $\phi^2 \in [0, \infty]$ per particle for $\gamma = 0.1$ and $Sc = 1$. Computed values and values predicted by the model are compared in FIG. 25 for the first sphere, FIG. 26 for the second sphere and FIG. 27 for the third sphere. We also compare the mean volume concentration $\overline{C_v}$ in FIG. 28 for the first sphere, FIG. 29 for the second sphere and FIG. 30 for the third sphere. In general, the agreement between computed values and values predicted by the model is once again deemed to be satisfactory. The Damkohler number ϕ^2 has the most significant impact on the observed difference between computed values and model predictions. For $\phi^2 < 200$, the agreement in very satisfactory for all spheres and the observed difference is very small. Then for larger $\phi^2 > 200$, the observed difference, though still limited,

increases with ϕ^2. The maximum difference of the order of 10% is attained for $\phi^2 = 4000$. As pointed out in the above, this trend is related to the internal concentration boundary layer that decreases with the increase of the Thiele modulus as $1/\phi$. The same comments apply to the plots of the reactive Sherwood numbers given by (59) for the 3 spheres in FIG. 32 for the first sphere, FIG. 33 for the second sphere and FIG. 34 for the third sphere.

The observed differences between computed values of $\overline{C_s}$, $\overline{C_v}$ or $\widetilde{Sh}$ and the values of the same quantities predicted by the model have 3 sources:

1. approximations and assumptions adopted to derive the model,
2. not fully converged in space computed solutions for large values of ϕ^2,
3. correlations proposed for the coefficients β_j by Ramachandran et al. (1989) and established by a least square regression with a maximum error of 2.5% for β_1, 4.6% for β_2 and 10% for β_3.

In the case of the 3 aligned spheres, the equivalent solid volume fraction around the spheres is low and the system is representative of a dilute regime. The interactions between the 3 spherical obstacles, both in terms of momentum and mass transfer, are limited, though far from negligible. As a result, the chemical concentration does not vary much along each sphere surface as shown in FIG. 31. Consequently, the approximations (51)-(52) to calculate the mean volume concentration, i.e., assuming that C is a function of the radial coordinate only and $C_s(\theta, \phi)$ does not vary too much around $\overline{C_s}$, are valid. The model is assumed to perform well in this flow configuration and this range of dimensionless parameters. So we believe that source 1 does not contribution much to the observed differences. The increase of the observed differences as a function of the Damkolher number ϕ^2 is certainly a sign that for high ϕ^2, $N_p = 70$ points per diameter might not yet be enough to yield fully spatially converged computed solutions as the internal boundary layer is getting thinner with the increase of ϕ^2, as suggested by FIG. 7 and FIG. 14. Source 2 is thereby a significant contribution to the observed differences at high ϕ^2. Finally, the magnitude of the error on the coefficients β_j as reported by Ramachandran et al. (1989) is of the same order as the observed

differences, so we cannot rule out the contribution of source 3. Overall, the model performs well. The difference between computed values and model predictions increases with the Damkohler number ϕ but is capped to 10% in the range of dimensionless parameters investigated.

6. Discussion and perspectives

We presented a numerical framework that couples a Sharp Interface Method (SIM) for the convection-diffusion-reaction conservation equation of the chemical species to a DLM/FD method to solve the incompressible Navier-Stokes equations with fixed obstacles. We presented multiple validation tests of growing complexity to ensure that our implementation of our DLM/FD-SIM method supplies computed solution with the expected accuracy. We have shown through various convergence tests, comparisons to analytical solutions, comparisons to correlations and comparisons to body-fitted simulations that our numerical tool indeed supplies reliable computed solutions. We then used our numerical tool to examine the problem of convective-diffusive mass transfer in the flow past 3 reactive spheres.

The primary objective of the work was to show that a reactive Sherwood number correlation can be constructed in a dilute system on the basis on a simple external-internal coupling and the additivity rule, in a similar way as we constructed a reactive Sherwood number correlation for a single isolated sphere in Sulaiman et al. (2018). Model predictions show a satisfactory agreement with our DLM/FD-SIM numerical results for wide ranges of the 4 governing parameters in the problem of convective-diffusive mass transfer in the flow past 3 reactive spheres. We consider this problem as an adequate toy model of a dilute particle-laden system experiencing hydrodynamic interactions. The strength of our reactive Sherwood number correlation is that it is based on any existing non-reactive Sherwood number correlation. Here we used the non-reactive Sherwood number correlations of Feng and Michaelides (2000) and Ramachandran et al. (1989), but this is not mandatory.

The ultimate objective is to extend the suggested reactive Sherwood number correlation to denser regime and eventually to use it in larger scale numerical models as

Euler/Lagrange and Euler/Euler modelling of reactive particle-laden flows. This can be achieved in 2 complementary ways. The former way involves investigating pairwise interactions in terms of reactive mass transfer. A model system would be the flow past 2 spheres not aligned with the flow and then investigate not only the effect of the inter-particle distance but also of the relative angular position of the 2 particles, in a similar way to Akiki et al. (2017) for momentum transfer. The latter way involves computing the flow through a random array of reactive spheres up to a high solid volume fraction α_s close to packing, as illustrated in FIG. 35. This would require large computing resources to span all parameter ranges but is feasible as our code is fully parallel and can run on large supercomputers with a satisfactory scalability. This work is currently under way.

Appendices

A. Derivation of the diffusive Sherwood number in a finite spherical domain

We consider a sphere of radius r_p^* at concentration $C = C_s|_{r^*=r_p^*}$ at the center of a spherical domain of radius $r^* = r_\infty^*$ filled with a quiescent fluid of diffusion coefficient D_f^*. At steady state, the concentration distribution C in the fluid is governed by:

$$D_f^* \nabla^2 C = 0 \tag{61}$$

(61) can easily be integrated with the two Dirichlet boundary conditions $C = C_s|_{r^*=r_p^*}$ and $C = C_\infty|_{r^*=r_\infty^*}$. The solution, i.e., the concentration profile $C(r^*)$ in the fluid phase, reads:

$$C(r^*) = \frac{r_p^* r_\infty^*}{(r_p^* - r_\infty^*)r^*}(C_\infty - C_s) + \frac{C_s r_p^* - C_\infty r_\infty^*}{r_p^* - r_\infty^*} \tag{62}$$

The mass transfer coefficient k^* can be calculated through the calculation of the total flux through the sphere surface as:

$$k^* = \frac{D_f^*}{4\pi r_p^{*2}(C_\infty - C_s)} \int_0^{2\pi} \int_{-\pi/2}^{+\pi/2} \left.\frac{\partial C(r^*)}{\partial r^*}\right|_{r^*=r_p^*} r_p^{*2} sin(\theta) d\phi d\theta \tag{63}$$

Substituting (62) into (63), the diffusive Sherwood number in a finite spherical domain $Sh = \dfrac{k^* d_p^*}{D_f^*}$ can be written as:

$$Sh = \frac{k^* d_p^*}{D_f^*} = \frac{2r_\infty^*}{r_\infty^* - r_p^*} \tag{64}$$

For an infinite domain, i.e., when $r_\infty^* \to \infty$, $Sh \to 2$. For a spherical domain of finite size, Sh is larger than 2 and its value can be calculated by (64).

References

Akiki, G., Jackson, T., Balachandar, S., 2017. Pairwise interaction extended point-particle model for a random array of monodisperse spheres. Journal of Fluid Mechanics 813, 882–928.

Augier, F., Idoux, F., Delenne, J.Y., 2010a. Numerical simulations of transfer and transport properties inside packed beds of spherical particles. Chemical Engineering Science 65, 1055–1064.

Augier, F., Koudil, A., Royon-Lebeaud, A., Muszynski, L., Yanouri, Q., 2010b. Numerical approach to predict wetting and catalyst efficiencies inside trickle bed reactors. Chemical Engineering Science 65, 255–260.

Calmet, I., Magnaudet, J., 1997. Large-eddy simulation of high-schmidt number mass transfer in a turbulent channel flow. Physics of Fluids 9, 438–455.

Clift, R., Grace, J.R., Weber, M.E., 2005. Bubbles, drops, and particles. Courier Corporation.

Dan, C., Wachs, A., 2010. Direct numerical simulation of particulate flow with heat transfer. International Journal of Heat and Fluid Flow 31, 1050–1057.

Deen, N.G., Peters, E., Padding, J.T., Kuipers, J., 2014. Review of direct numerical simulation of fluid–particle mass, momentum and heat transfer in dense gas–solid flows. Chemical Engineering Science 116, 710–724.

Dorai, F., Moura Teixeira, C., Rolland, M., Climent, E., Marcoux, M., Wachs, A., 2015. Fully resolved simulations of the flow through a packed bed of cylinders: Effect of size distribution. Chemical Engineering Science 129, 180–192.

Duarte, F., Gormaz, R., Natesan, S., 2004. Arbitrary lagrangian–eulerian method for navier–stokes equations with moving boundaries. Computer Methods in Applied Mechanics and Engineering 193, 4819–4836.

Fedkiw, R.P., Aslam, T., Merriman, B., Osher, S., 1999. A non-oscillatory eulerian approach to interfaces in multimaterial flows (the ghost fluid method). Journal of computational physics 152, 457–492.

Feng, Z.G., Michaelides, E.E., 2000. A numerical study on the transient heat transfer from a sphere at high reynolds and peclet numbers. International Journal of Heat and Mass Transfer 43, 219–229.

Furuta, S., Matsuhashi, H., Arata, K., 2006. Biodiesel fuel production with solid amorphous-zirconia catalysis in fixed bed reactor. Biomass and Bioenergy 30, 870–873.

Gibou, F., Fedkiw, R., Caflisch, R., Osher, S., 2003. A level set approach for the numerical simulation of dendritic growth. Journal of Scientific Computing 19, 183–199.

Gibou, F., Fedkiw, R.P., Cheng, L.T., Kang, M., 2002. A second-order-accurate symmetric discretization of the poisson equation on irregular domains. Journal of Computational Physics 176, 205–227.

Gidaspow, D., 1994. Multiphase flow and fluidization: continuum and kinetic theory descriptions. Academic press.

Glowinski, R., Pan, T., Hesla, T., Joseph, D., Periaux, J., 2001. A fictitious domain approach to the direct numerical simulation of incompressible viscous flow past moving rigid bodies: application to particulate flow. Journal of Computational Physics 169, 363–426.

Glowinski, R., Pan, T.W., Hesla, T.I., Joseph, D.D., 1999. A distributed lagrange multiplier/fictitious domain method for particulate flows. International Journal of Multiphase Flow 25, 755–794.

Gunn, D., 1978. Transfer of heat or mass to particles in fixed and fluidised beds. International Journal of Heat and Mass Transfer 21, 467–476.

Haroun, Y., Legendre, D., Raynal, L., 2010. Volume of fluid method for interfacial reactive mass transfer: application to stable liquid film. Chemical Engineering Science 65, 2896–2909.

Hu, H.H., Patankar, N.A., Zhu, M., 2001. Direct numerical simulations of fluid–solid systems using the arbitrary lagrangian–eulerian technique. Journal of Computational Physics 169, 427–462.

Kang, M., Fedkiw, R.P., Liu, X.D., 2000. A boundary condition capturing method for multiphase incompressible flow. Journal of Scientific Computing 15, 323–360.

Kapahi, A., Mousel, J., Sambasivan, S., Udaykumar, H., 2013. Parallel, sharp interface eulerian approach to high-speed multi-material flows. Computers & Fluids 83, 144–156.

Khiabani, R.H., Joshi, Y., Aidun, C.K., 2010. Heat transfer in microchannels with suspended solid particles: lattice-boltzmann based computations. Journal of Heat Transfer 132, 041003.

Kruggel-Emden, H., Kravets, B., Suryanarayana, M., Jasevicius, R., 2016. Direct numerical simulation of coupled fluid flow and heat transfer for single particles and particle packings by a lbm-approach. Powder Technology 294, 236–251.

Liu, H., Krishnan, S., Marella, S., Udaykumar, H., 2005. Sharp interface cartesian grid method ii: A technique for simulating droplet interactions with surfaces of arbitrary shape. Journal of Computational Physics 210, 32–54.

Liu, X.D., Fedkiw, R.P., Kang, M., 2000. A boundary condition capturing method for poisson's equation on irregular domains. Journal of computational Physics 160, 151–178.

Lu, J., Das, S., Peters, E., Kuipers, J., 2018. Direct numerical simulation of fluid flow and mass transfer in dense fluid-particle systems with surface reactions. Chemical Engineering Science 176, 1–18.

Magnaudet, J., Rivero, M., Fabre, J., 1995. Accelerated flows past a rigid sphere or a spherical bubble. part 1. steady straining flow. Journal of fluid mechanics 284, 97–135.

Marella, S., Krishnan, S., Liu, H., Udaykumar, H., 2005. Sharp interface cartesian grid method i: an easily implemented technique for 3d moving boundary computations. Journal of Computational Physics 210, 1–31.

Maxwell, J.C., Garnett, W., Pesic, P., 2005. An elementary treatise on electricity. Courier Corporation.

Montero, C., Remiro, A., Benito, P.L., Bilbao, J., Gayubo, A.G., 2018. Optimum operating conditions in ethanol steam reforming over a ni/la 2 o 3-αal 2 o 3 catalyst in a fluidized bed reactor. Fuel Processing Technology 169, 207–216.

Rahmani, M., Wachs, A., 2014. Free falling and rising of spherical and angular particles. Physics of Fluids 26, 083301.

Ramachandran, R., Kleinstreuer, C., Wang, T.Y., 1989. Forced convection heat transfer of interacting spheres. Numerical heat transfer 15, 471–487.

Ranz, W., Marshall, W., et al., 1952. Evaporation from drops. Chem. Eng. Prog 48, 141–146.

Romkes, S., Dautzenberg, F., Van den Bleek, C., Calis, H., 2003. Cfd modelling and experimental validation of particle-to-fluid mass and heat transfer in a packed bed at very low channel to particle diameter ratio. Chemical Engineering Journal 96, 3–13.

Shao, X., Shi, Y., Yu, Z., 2012. Combination of the fictitious domain method and the sharp interface method for direct numerical simulation of particulate flows with heat transfer. International Journal of Heat and Mass Transfer 55, 6775–6785.

Shi, Y., Yu, Z., Shao, X., 2011. Combination of the direct-forcing fictitious domain method and the sharp interface method for the three-dimensional dielectrophoresis of particles. Powder technology 210, 52–59.

Sulaiman, M., Climent, E., Hamoutti, A., Wachs, A., 2018. Mass transfer towards a reactive particle in a fluid flow : numerical simulations and modeling. Chemical Engineering Science 65, 1055–1064.

Sun, B., Tenneti, S., Subramaniam, S., 2015. Modeling average gas–solid heat transfer using particle-resolved direct numerical simulation. International Journal of Heat and Mass Transfer 86, 898–913.

Sun, B., Tenneti, S., Subramaniam, S., Koch, D.L., 2016. Pseudo-turbulent heat flux and average gas–phase conduction during gas–solid heat transfer: flow past random fixed particle assemblies. Journal of Fluid Mechanics 798, 299–349.

Udaykumar, H., Mao, L., 2002. Sharp-interface simulation of dendritic solidification of solutions. International journal of heat and mass transfer 45, 4793–4808.

Uhlmann, M., 2005. An immersed boundary method with direct forcing for the simulation of particulate flows. Journal of Computational Physics 209, 448–476.

Wachs, A., 2011. Rising of 3d catalyst particles in a natural convection dominated flow by a parallel dns method. Computers & Chemical Engineering 35, 2169–2185.

Wachs, A., Hammouti, A., Vinay, G., Rahmani, M., 2015. Accuracy of finite volume/staggered grid distributed lagrange multiplier/fictitious domain simulations of particulate flows. Computers & Fluids 115, 154–172.

Whitaker, S., 1972. Forced convection heat transfer correlations for flow in pipes, past flat plates, single cylinders, single spheres, and for flow in packed beds and tube bundles. AIChE Journal 18, 361–371.

Xia, J., Luo, K., Fan, J., 2014. A ghost-cell based high-order immersed boundary method for inter-phase heat transfer simulation. International Journal of Heat and Mass Transfer 75, 302–312.

Yu, Z., Shao, X., Wachs, A., 2006. A fictitious domain method for particulate flows with heat transfer. Journal of Computational Physics 217, 424–452.

List of Figures

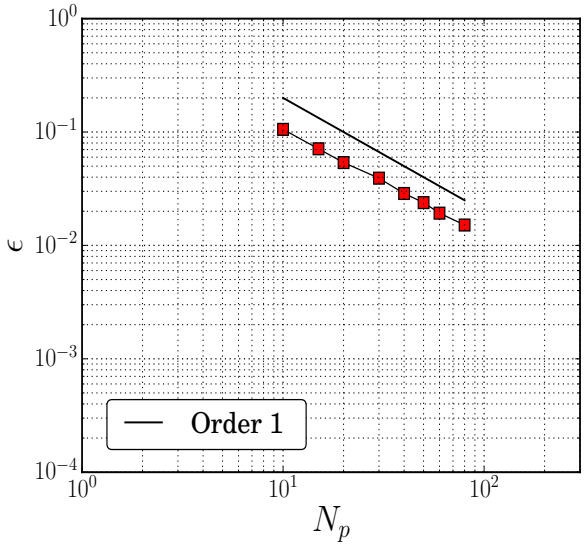

Figure 1: Steady state diffusion from a single particle in a finite domain $L_x = L_y = L_z = 10$: spatial convergence of the error on the Sherwood number computed with SIM compared to the analytical solution.

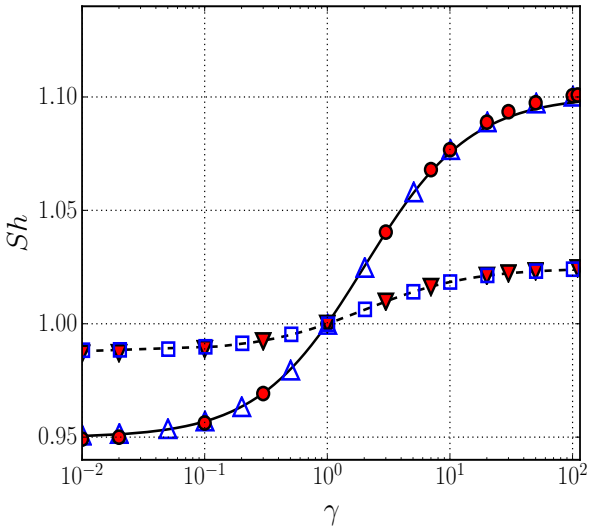

Figure 2: Steady state diffusion from a single particle in a gradient of concentration: comparison of average Sherwood number computed with SIM to the analytical solution and to the previous study of Shao et al. (2012). Case 1, $r_p^*/L_x^* = 0.2$: continuous black line corresponds to the analytical solution, open triangles correspond to the results of Shao et al. (2012), and disks correspond to our simulation results. Case 2, $r_p^*/L_x^* = 0.125$: dashed black line corresponds to the analytical solution, open squares correspond to the results of Shao et al. (2012) and triangles correspond to our simulation results.

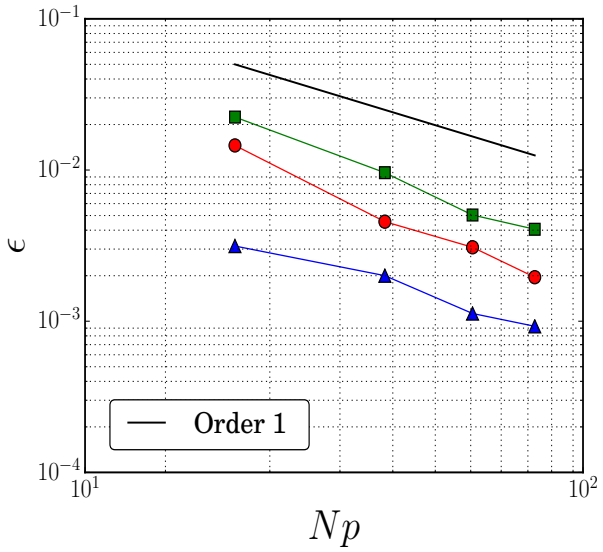

Figure 3: Steady state diffusion from a single particle in a gradient of concentration: spatial convergence of the relative error on the average Sherwood number computed with SIM. Triangles correspond to $r_p^*/L_x^* = 0.1$, disks correspond to $r_p^*/L_x^* = 0.125$, and squares correspond $r_p^*/L_x^* = 0.2$.

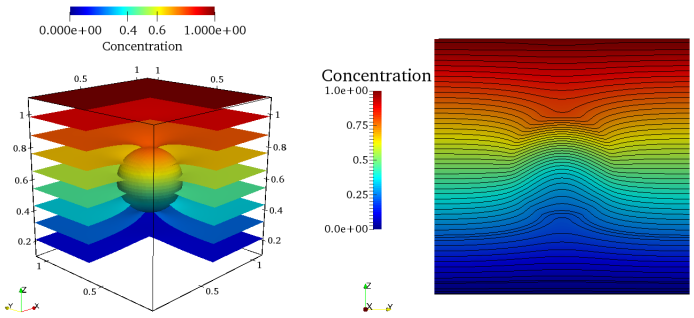

Figure 4: Steady state diffusion from a single particle in a gradient of concentration: concentration iso-countours for $r_p^*/L_x^* = 0.2$ and $\gamma = 0.1$ in a 3D view (left) and in a xz vertical cut plane containing the sphere center (right).

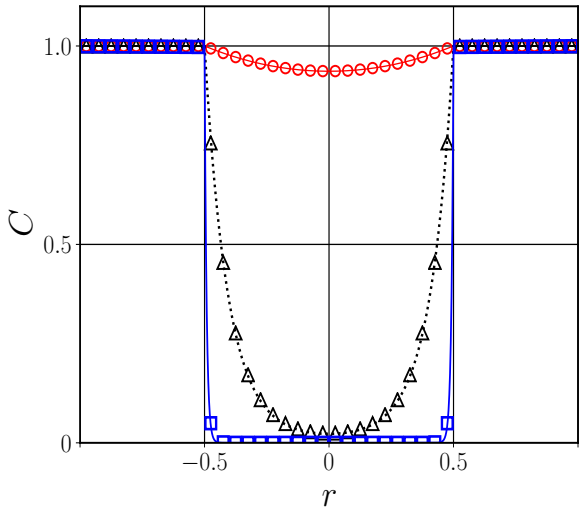

Figure 5: Internal diffusion and chemical reaction in a single particle: comparison of concentration profiles computed with SIM to analytical profiles for different Thiele moduli. Lines correspond to analytical solutions and markers correspond to our simulation results. Red line and red circles for $\phi^2 = 1.6$. Black doted line and open triangles for $\phi^2 = 160$. Blue line and open squares for $\phi^2 = 16000$.

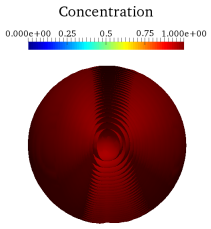

(a) $\phi^2 = 1.6$

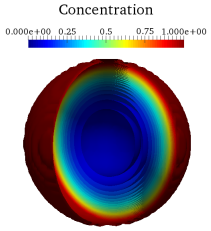

(b) $\phi^2 = 160$

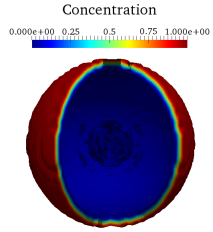

(c) $\phi^2 = 16000$

Figure 6: Internal diffusion and chemical reaction in a single particle: concentration iso-surfaces inside the particle for different reaction rates.

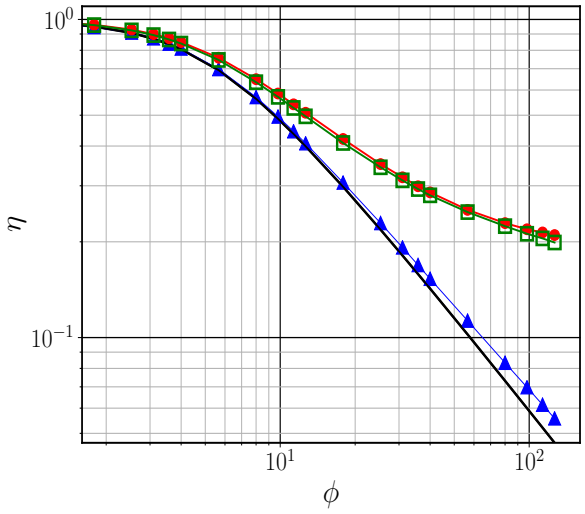

Figure 7: Internal diffusion and chemical reaction in a single particle: comparison of effectiveness factor computed with VOF and SIM as a function of ϕ. Red color corresponds to VOF obtained with $N_p = 40$ and green color corresponds to SIM obtained with $N_p = 10$. Blue color corresponds to SIM with $N_p = 80$ and black line corresponds to the analytical solution.

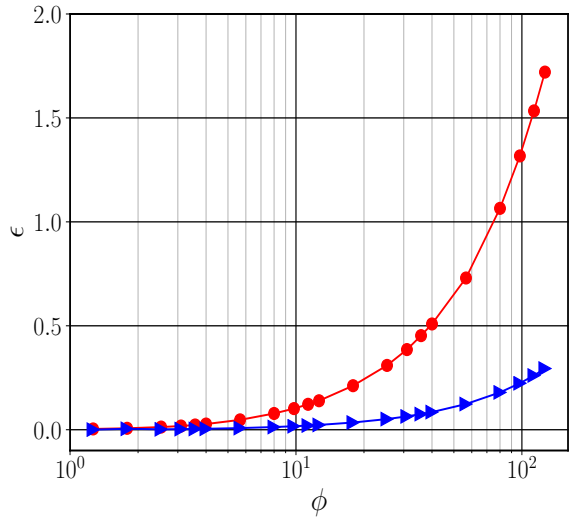

Figure 8: Internal diffusion and chemical reaction in a single particle: relative error on the effectiveness factor as a function of ϕ for $N_p = 80$. Red color corresponds to VOF and blue color corresponds to SIM.

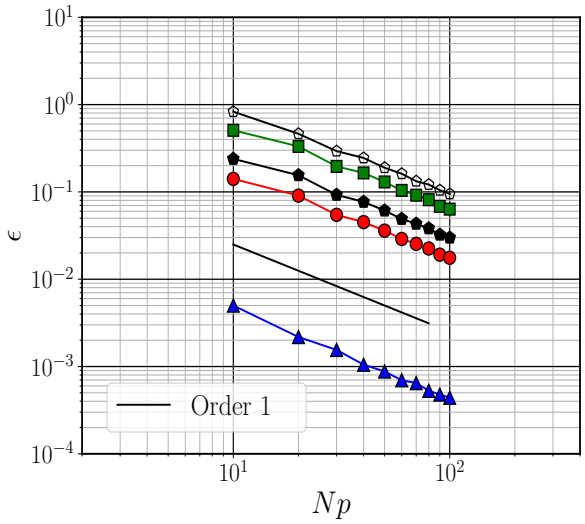

Figure 9: Internal diffusion and chemical reaction in a single particle: spatial convergence of relative error on effectiveness factor computed with SIM and VOF for various Thiele moduli: $\phi = 1.2$, blue triangles with SIM, $\phi = 12$, red disks with SIM, $\phi = 20$, black filled pentagons with SIM, black open pentagons with VOF, $\phi = 120$, green squares with SIM.

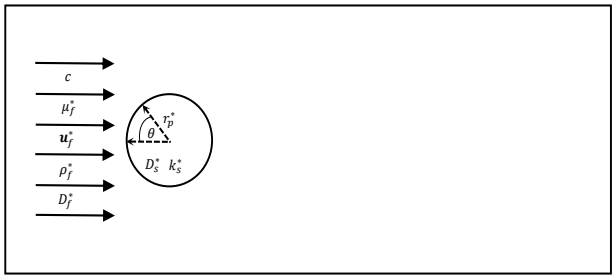

Figure 10: Geometric configuration for the problem of steady state convection-diffusion in the flow past a single sphere with or without reaction inside the particle: view in a xz cut plane containing the sphere center (Simulation domain is $5d_p^* \times 5d_p^* \times 15d_p^*$).

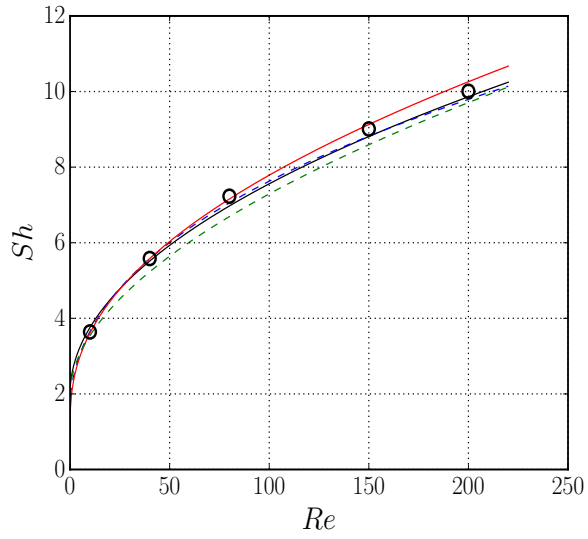

Figure 11: Steady state convection-diffusion in the flow past a single sphere: comparison of computed Sherwood number with literature correlations at $Sc = 1$. Our SIM results are represented by circles while correlations are as follows: red line for Feng and Michaelides (2000), black line for Ranz et al. (1952), green-doted line for Whitaker (1972) and blue-dashed line for Clift et al. (2005).

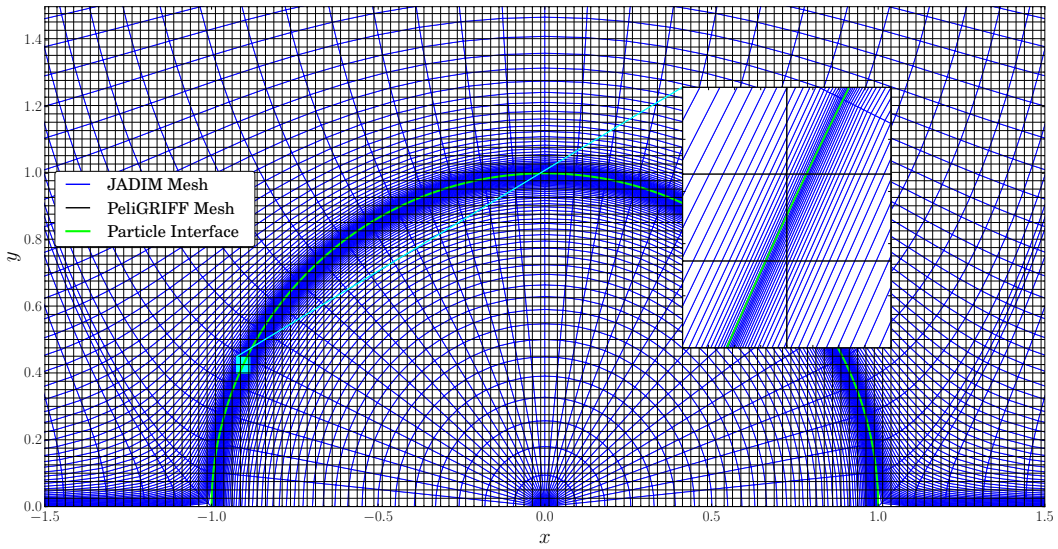

Figure 12: Comparison of the finest meshes used by JADIM (boundary fitted) and SIM (cartesian grid).

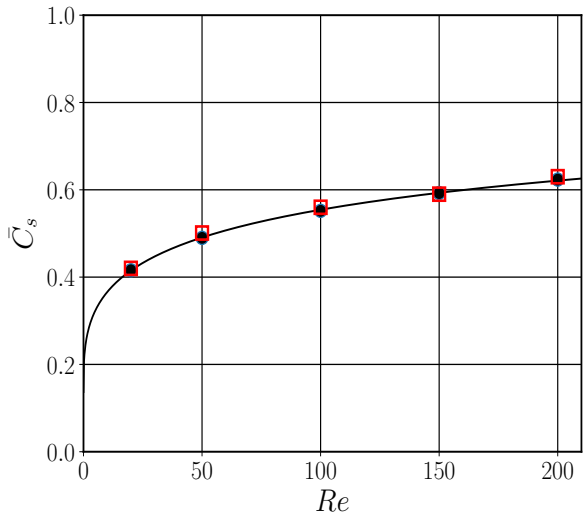

Figure 13: Steady state convection-diffusion in the flow past a single reactive sphere: comparison of the mean surface concentration $\overline{C_s}$ at $\phi = 2$, $\gamma = 10$ and $Sc = 1$ as a function of Re, computed with SIM (red squares), computed with JADIM (black disks), and predicted by the model of Sulaiman et al. (2018) (black line).

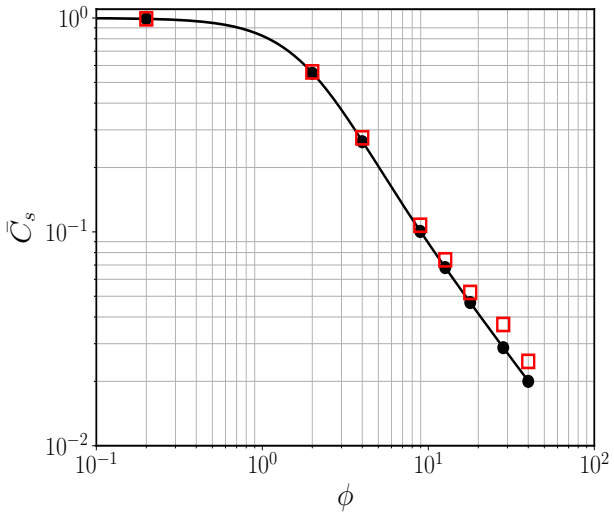

Figure 14: Steady state convection-diffusion in the flow past a single reactive sphere: comparison of mean surface concentration $\overline{C_s}$ at $Re = 150$, $\gamma = 10$ and $Sc = 1$ as a function of ϕ, computed with SIM (red squares), computed with JADIM (black disks), and predicted by the model of Sulaiman et al. (2018) (black line).

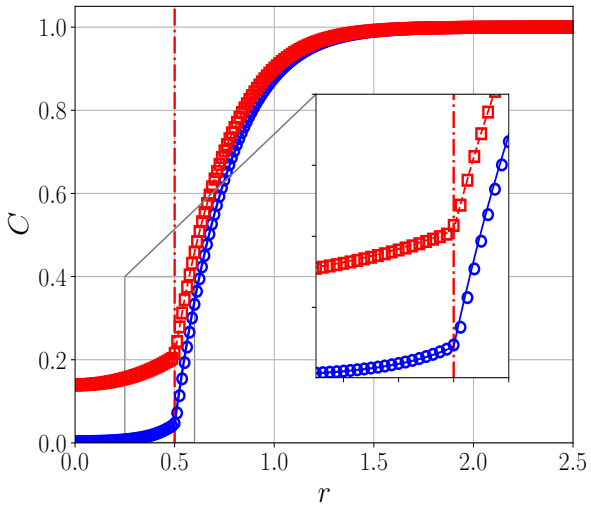

Figure 15: Steady state convection-diffusion in the flow past a single reactive sphere: comparison of concentration profile in the direction normal to the flow ($\theta = 90$), at $Re = 10$, $\gamma = 10$ and $Sc = 1$ for two Thiele moduli: $\phi = 4$, red color, and $\phi = 10$, blue color. Continuous line correspond to JADIM and markers correspond to SIM.

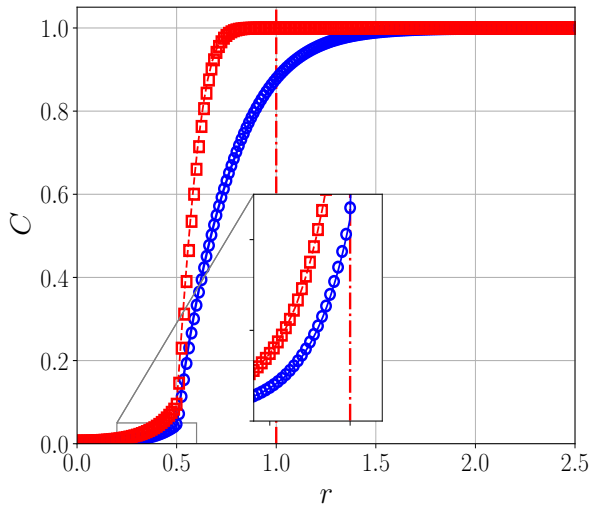

Figure 16: Steady state convection-diffusion in the flow past a single reactive sphere: comparison of concentration profile in the direction normal to the flow ($\theta = 90$), for $\phi = 4$, $\gamma = 10$ and $Sc = 1$ and two Reynolds numbers: $Re = 100$, red color, and $Re = 10$, blue color. Continuous lines correspond to JADIM and markers correspond to SIM.

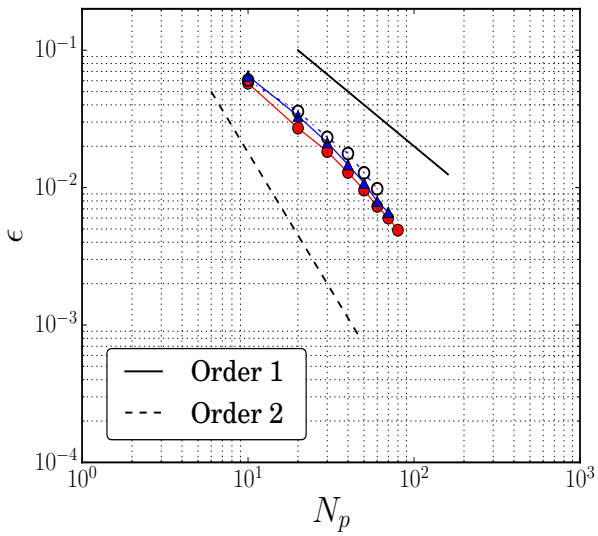

Figure 17: Steady state convection-diffusion in the flow past a single reactive sphere: spatial convergence of relative error on mean surface concentration $\overline{C_s}$ computed with SIM at $Re = 150$, $\phi^2 = 40$, and $\gamma = 0.1$ for $Sc = 0.1$, red disks, $Sc = 1$, black triangles, and $Sc = 10$, black open circles.

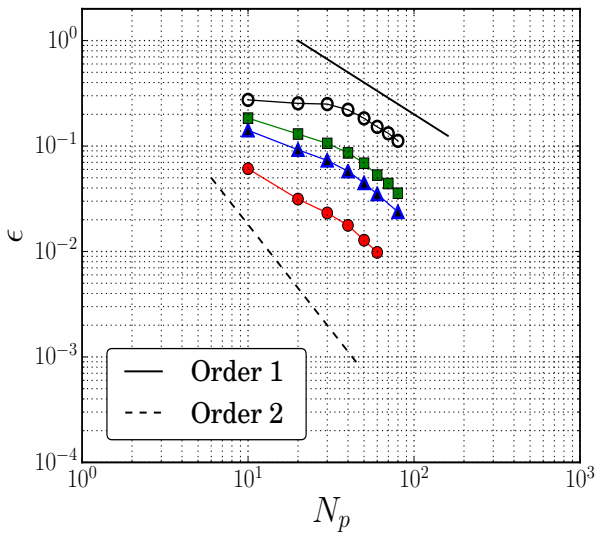

Figure 18: Steady state convection-diffusion in the flow past a single reactive sphere: spatial convergence of relative error on mean surface concentration $\overline{C_s}$ computed with SIM at $Re = 150$, $Sc = 10$, and $\gamma = 0.1$ for $\phi^2 = 40$, red disks, $\phi^2 = 200$, blue triangles, $\phi^2 = 400$, green squares, and $\phi^2 = 4000$, black open circles.

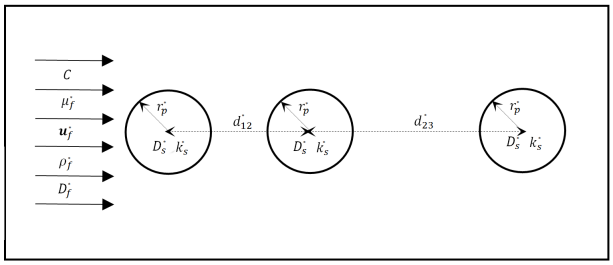

Figure 19: Geometric configuration for the problem of steady state convection-diffusion in the flow past 3 aligned reactive spheres: view in a xz cut plane containing the sphere center (Simulation domain is $5d_p^* \times 5d_p^* \times 15d_p^*$).

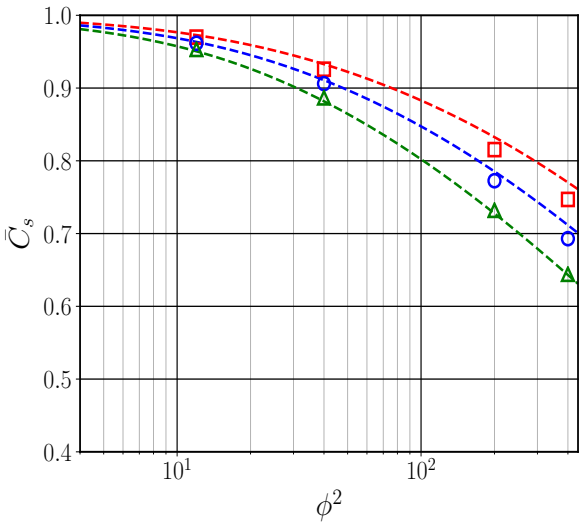

Figure 20: Steady state convection-diffusion in the flow past 3 aligned reactive spheres: mean surface concentration $\overline{C_s}$ as a function of ϕ^2 in configuration A at $Re = 50$, $Sc = 1$ and $\gamma = 0.1$. Lines correspond to model and markers correspond to SIM. Red color corresponds to first sphere, blue color to second sphere and green color corresponds to third sphere.

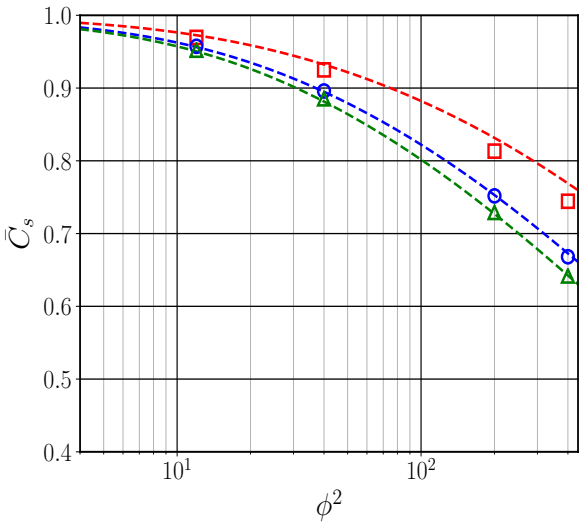

Figure 21: Steady state convection-diffusion in the flow past 3 aligned reactive spheres: mean surface concentration $\overline{C_s}$ as a function of ϕ^2 in configuration B at $Re = 50$, $Sc = 1$ and $\gamma = 0.1$. Lines correspond to model and markers correspond to SIM. Red color corresponds to first sphere, blue color to second sphere and green color corresponds to third sphere.

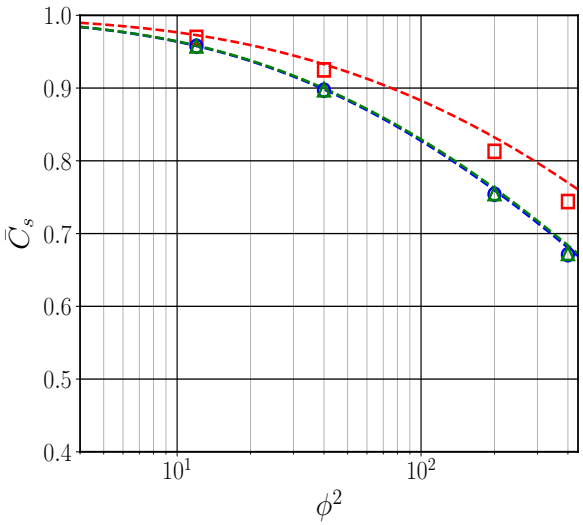

Figure 22: Steady state convection-diffusion in the flow past 3 aligned reactive spheres: mean surface concentration $\overline{C_s}$ as a function of ϕ^2 in configuration C at $Re = 50$, $Sc = 1$ and $\gamma = 0.1$. Lines correspond to model and markers correspond to SIM. Red color corresponds to first sphere, blue color to second sphere and green color corresponds to third sphere.

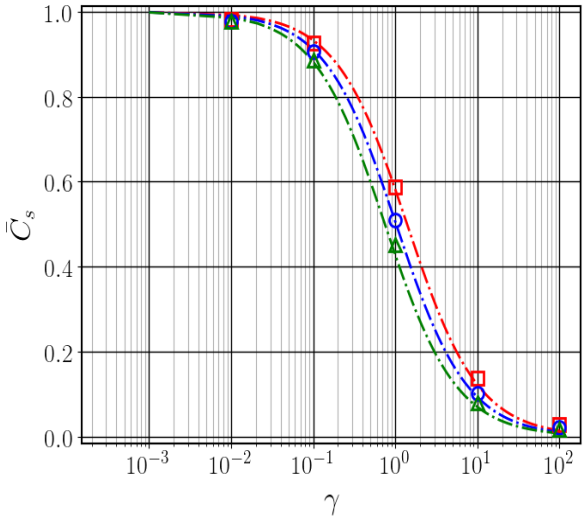

Figure 23: Steady state convection-diffusion in the flow past 3 aligned reactive spheres: mean surface concentration $\overline{C_s}$ as a function of γ in configuration A at $Re = 50$, $Sc = 1$ and $\phi^2 = 40$. Lines correspond to model and markers correspond to SIM. Red color corresponds to first sphere, blue color to second sphere and green color corresponds to third sphere.

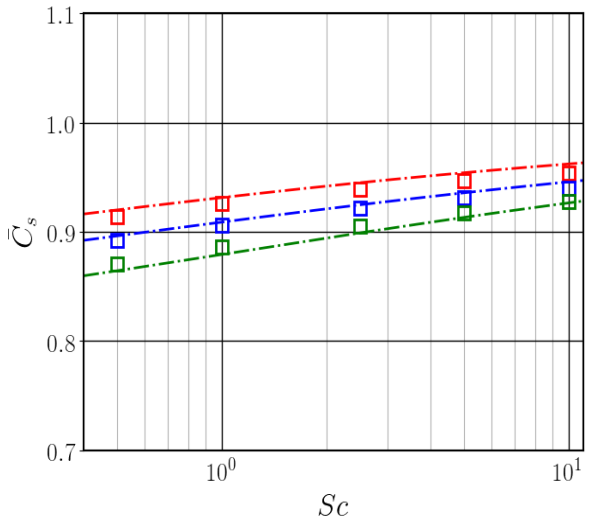

Figure 24: Steady state convection-diffusion in the flow past 3 aligned reactive spheres: mean surface concentration $\overline{C_s}$ as a function of Sc in configuration A at $\phi^2 = 40$, $Re = 50$ and $\gamma = 0.1$. Lines correspond to model and markers correspond to SIM. Red color corresponds to first sphere, blue color to second sphere and green color corresponds to third sphere.

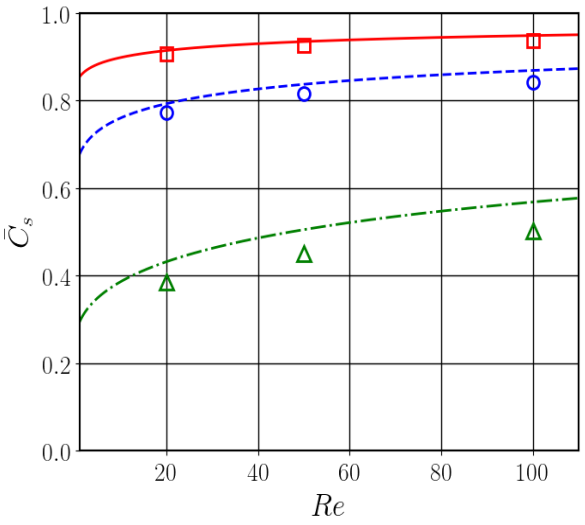

Figure 25: Steady state convection-diffusion in the flow past 3 aligned reactive spheres: mean surface concentration $\overline{C_s}$ of sphere 1 as a function of Re in configuration A at $\gamma = 0.1$ and $Sc = 1$. Lines correspond to model and markers correspond to numerical simulation. Red color corresponds to $\phi^2 = 40$, blue color to $\phi^2 = 200$ and green color corresponds to $\phi^2 = 4000$.

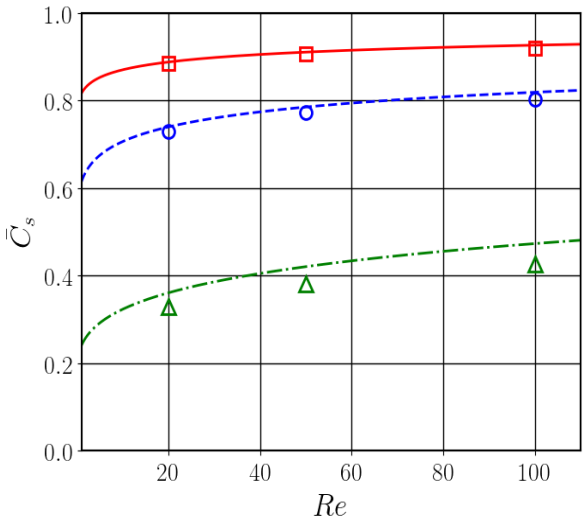

Figure 26: Steady state convection-diffusion in the flow past 3 aligned reactive spheres: mean surface concentration $\overline{C_s}$ of sphere 2 as a function of Re in configuration A at $\gamma = 0.1$ and $Sc = 1$. Lines correspond to model and markers correspond to numerical simulation. Red color corresponds to $\phi^2 = 40$, blue color to $\phi^2 = 200$ and green color corresponds to $\phi^2 = 4000$.

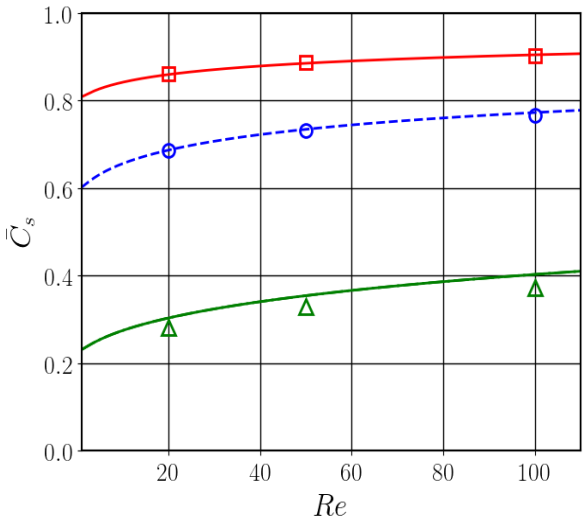

Figure 27: Steady state convection-diffusion in the flow past 3 aligned reactive spheres: mean surface concentration $\overline{C_s}$ of sphere 3 as a function of Re in configuration A at $\gamma = 0.1$ and $Sc = 1$. Lines correspond to model and markers correspond to numerical simulation. Red color corresponds to $\phi^2 = 40$, blue color to $\phi^2 = 200$ and green color corresponds to $\phi^2 = 4000$.

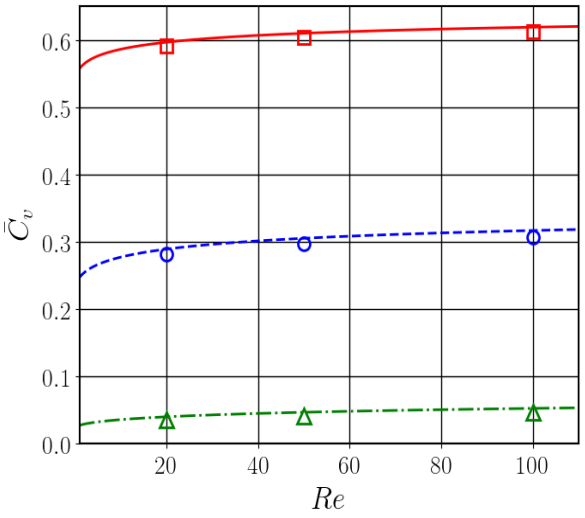

Figure 28: Steady state convection-diffusion in the flow past 3 aligned reactive spheres: mean volume concentration $\overline{C_v}$ of sphere 1 as a function of Re in configuration A at $\gamma = 0.1$ and $Sc = 1$. Lines correspond to model and markers correspond to numerical simulation. Red color corresponds to $\phi^2 = 40$, blue color to $\phi^2 = 200$ and green color corresponds to $\phi^2 = 4000$.

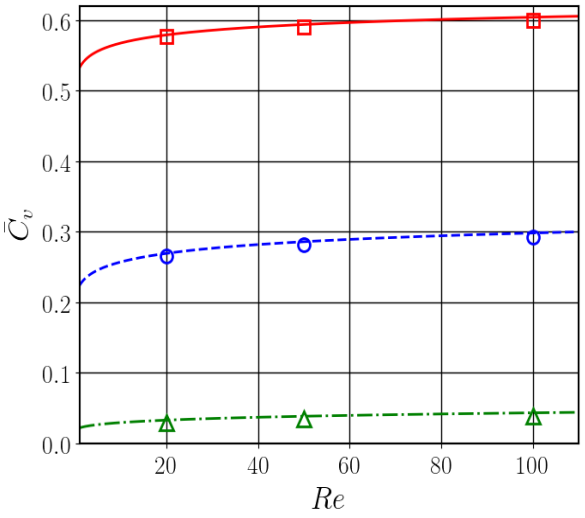

Figure 29: Steady state convection-diffusion in the flow past 3 aligned reactive spheres: mean volume concentration $\overline{C_v}$ of sphere 2 as a function of Re in configuration A at $\gamma = 0.1$ and $Sc = 1$. Lines correspond to model and markers correspond to numerical simulation. Red color corresponds to $\phi^2 = 40$, blue color to $\phi^2 = 200$ and green color corresponds to $\phi^2 = 4000$.

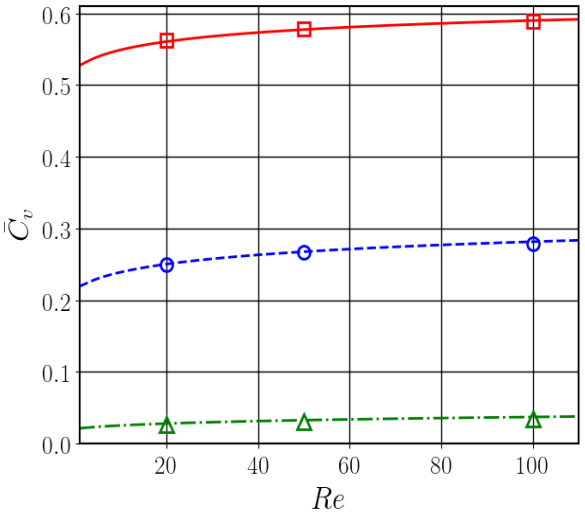

Figure 30: Steady state convection-diffusion in the flow past 3 aligned reactive spheres: mean volume concentration $\overline{C_v}$ of sphere 3 as a function of Re in configuration A at $\gamma = 0.1$ and $Sc = 1$. Lines correspond to model and markers correspond to numerical simulation. Red color corresponds to $\phi^2 = 40$, blue color to $\phi^2 = 200$ and green color corresponds to $\phi^2 = 4000$.

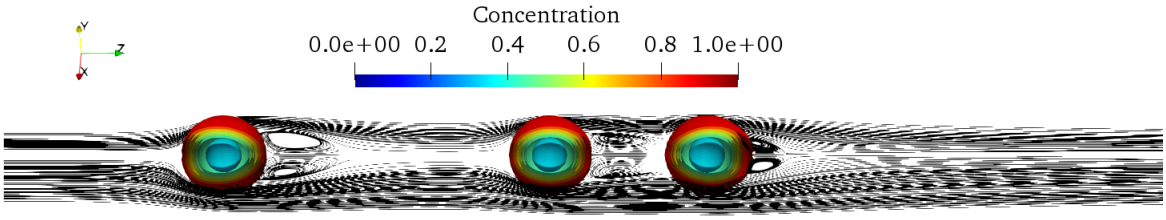

(a) $\phi^2 = 40$

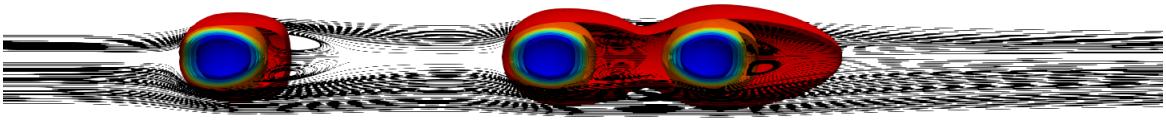

(b) $\phi^2 = 200$

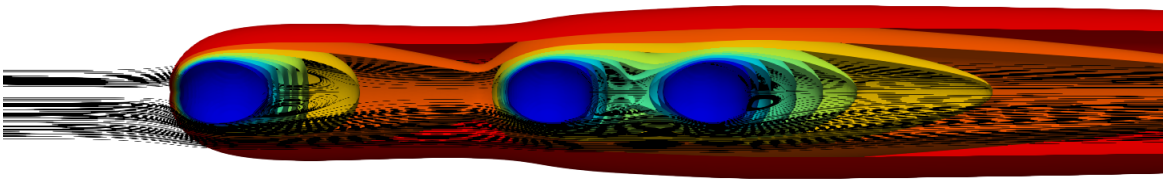

(c) $\phi^2 = \infty$

Figure 31: Steady state convection-diffusion in the flow past 3 aligned reactive spheres: concentration iso-surfaces in configuration A at $Re = 50$, $\gamma = 0.1$, $Sc = 1$ and different ϕ^2.

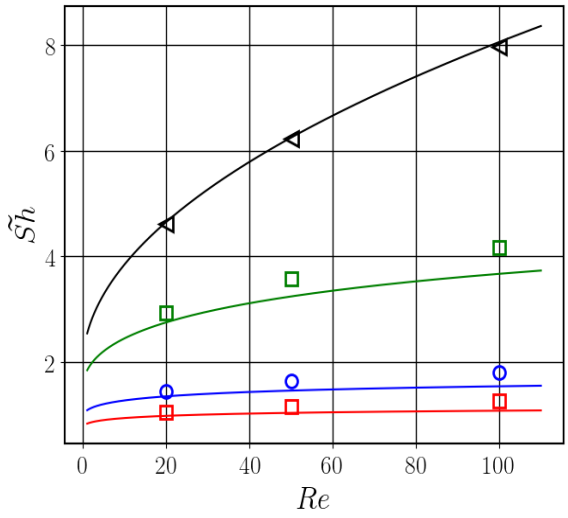

Figure 32: Steady state convection-diffusion in the flow past 3 aligned reactive spheres: reactive Sherwood number $\tilde{Sh}$ of sphere 1 as a function of Re in configuration A at $\gamma = 0.1$ and $Sc = 1$. Lines correspond to model and markers correspond to numerical simulation. Red color corresponds to $\phi^2 = 40$, blue color to $\phi^2 = 200$, green color correspond to $\phi^2 = 4000$ and black color corresponds to $\phi^2 = \infty$.

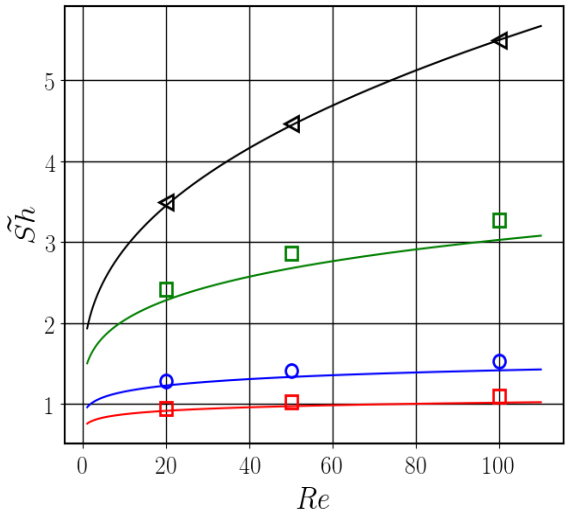

Figure 33: Steady state convection-diffusion in the flow past 3 aligned reactive spheres: reactive Sherwood number $\tilde{Sh}$ of sphere 2 as a function of Re in configuration A at $\gamma = 0.1$ and $Sc = 1$. Lines correspond to model and markers correspond to numerical simulation. Red color corresponds to $\phi^2 = 40$, blue color to $\phi^2 = 200$, green color corresponds to $\phi^2 = 4000$ and black color corresponds to $\phi^2 = \infty$.

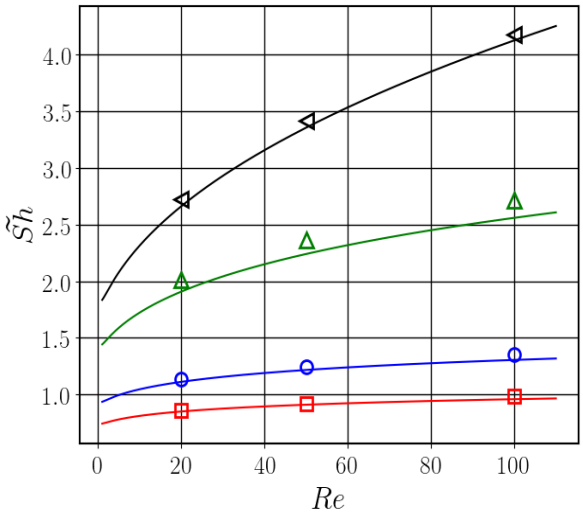

Figure 34: Steady state convection-diffusion in the flow past 3 aligned reactive spheres: reactive Sherwood number $\tilde{Sh}$ of sphere 3 as a function of Re in configuration A at $\gamma = 0.1$ and $Sc = 1$. Lines correspond to model and markers correspond to numerical simulation. Red color corresponds to $\phi^2 = 40$, blue color to $\phi^2 = 200$, green color corresponds to $\phi^2 = 4000$ and black color corresponds to $\phi^2 = \infty$.

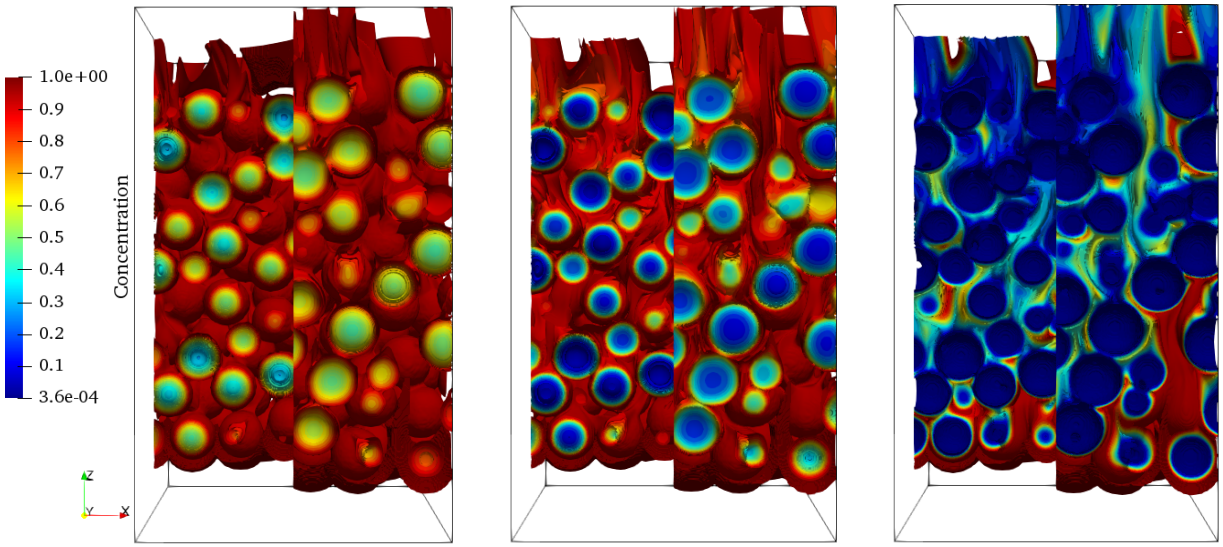

(a) $\phi^2 = 40$ **(b)** $\phi^2 = 200$ **(c)** $\phi^2 = \infty$

Figure 35: Concentration iso-surfaces in the the flow through a random array of spheres at $Re = 25$, $\gamma = 0.1$, $Sc = 1$, $\alpha_s = 0.5$ and different Damkohler numbers ϕ^2.